

Bachelor Thesis



**Czech
Technical
University
in Prague**

F3

**Faculty of Electrical Engineering
Department of Radioelectronics**

HW for Indoor Visible Light Positioning Testbed

Štěpán Bosák

**Supervisor: Ing. Stanislav Vitek, Ph.D.
May 2020**

I. Personal and study details

Student's name: **Bosák Štěpán** Personal ID number: **474230**
Faculty / Institute: **Faculty of Electrical Engineering**
Department / Institute: **Department of Radioelectronics**
Study program: **Electronics and Communications**

II. Bachelor's thesis details

Bachelor's thesis title in English:

HW for Indoor Visible Light Positioning Testbed

Bachelor's thesis title in Czech:

HW řešení systému pro navigaci uvnitř budov s využitím komunikace ve viditelném světle

Guidelines:

The aim of this work is to design a platform for testing algorithms for indoor navigation using visible light communication.

Follow these guidelines:

- 1) Introduce yourself with the algorithms of navigation using visible light communication
- 2) design and implement node of the navigation system
- 3) the node is a light source controlled by a microprocessor
- 4) individual nodes will communicate with the central unit via the LoRa network
- 5) Test the designed device under laboratory condition

Bibliography / sources:

- [1] CHAUDHARY, Neha; ALVES, Luis Nero; GHASSEMBLOOY, Zabih. Current Trends on Visible Light Positioning Techniques. In: 2019 2nd West Asian Colloquium on Optical Wireless Communications (WACOWC). IEEE, 2019. p. 100-105.
- [2] GONG, Chen. Visible Light Communication and Positioning: Present and Future. 2019.
- [3] XU, Jiaojiao; GONG, Chen; XU, Zhengyuan. Experimental indoor visible light positioning systems with centimeter accuracy based on a commercial smartphone camera. IEEE Photonics Journal, 2018, 10.6: 1-17.

Name and workplace of bachelor's thesis supervisor:

Ing. Stanislav Vitek, Ph.D., Department of Radioelectronics, FEE

Name and workplace of second bachelor's thesis supervisor or consultant:

Date of bachelor's thesis assignment: **03.02.2020** Deadline for bachelor thesis submission: _____

Assignment valid until: **30.09.2021**

Ing. Stanislav Vitek, Ph.D.
Supervisor's signature

doc. Ing. Josef Dobeš, CSc.
Head of department's signature

prof. Mgr. Petr Páta, Ph.D.
Dean's signature

III. Assignment receipt

The student acknowledges that the bachelor's thesis is an individual work. The student must produce his thesis without the assistance of others, with the exception of provided consultations. Within the bachelor's thesis, the author must state the names of consultants and include a list of references.

Date of assignment receipt

Student's signature

Acknowledgements

I would like to express my deep gratitude to Dr. Stanislav Vítek, my research supervisor, for his patient guidance, enthusiastic encouragement and useful critiques of this research work. I would also like to thank Ing. Jiří Náhlík, for his advice and assistance in the 3W LED driver analysis and prototyping. My grateful thanks are also extended to my colleague Martin Suda for his help and cooperation on the project. Special thanks should be given to Mr. Paul Gribbin for his professional language guidance and support.

Finally, I wish to thank my family and friends for their support and encouragement throughout my study.

Declaration

I declare that I have written submitted thesis by myself and that I have listed all information sources in accordance with Methodical Guideline on Compliance with Ethical Principles.

In Prague, 22 May 2020

Prohlašuji, že jsem předloženou práci vypracoval samostatně a že jsem uvedl veškeré použité informační zdroje v souladu s Metodickým pokynem o dodržování etických principů při přípravě vysokoškolských závěrečných prací.

V Praze, 22. května 2020

Abstract

This paper aims to design hardware for a testing environment for indoor navigation algorithms, which are using visible light. The first part focuses on gathering general knowledge about VLC (visible light communication) and VLC-based positioning systems. The main part is dedicated to designing an end node device, which consists of microcontroller NUCLEO-F446RE, expansion board for wireless radio communication using LoRaWAN technology I-NUCLEO-LRWAN1, high power LED driver and an electric power source. The final product is capable of modulating the LED (LEUWU1A301) with signals up to 10 kHz and the communication with the LoRaWAN network is verified in cooperation with M.Suda [1].

Keywords: Indoor navigation, visible light communication (VLC), end node device, microcontroller, LoRaWAN, LoRa, LED driver, light source

Supervisor: Ing. Stanislav Vítek, Ph.D.
Faculty of Electrical Engineering,
Technická 2,
160 00 Praha 6

Abstrakt

Cílem této práce je vytvoření hardwarového řešení pro testovací systém navigace uvnitř budov, který využívá komunikace ve viditelném světle. První část práce seznamuje se základními znalostmi o tomto typu komunikace a také s hlavními naváděcími metodami, které se v této oblasti uplatňují. Klíčová část práce je věnována designu světelného zdroje, který je zároveň tzv. koncovým zařízením v LoRaWAN síti. Navržené zařízení se skládá z mikrokontroléru NUCLEO-F446RE, rozšiřující desky I-NUCLEO-LRWAN1 umožňující LoRaWAN komunikaci, budiče vysokovýkonné LED a napětového zdroje. Výsledný produkt je schopen řízení LED diody (LEUWU1A301) signály do 10 kHz a ve spolupráci s M. Sudou [1] je otestováno připojení k LoRaWAN bráně a ověřena schopnost komunikace s LoRa sítí.

Klíčová slova: navigace uvnitř budov, komunikace pomocí viditelného světla, koncové zařízení, mikrokontrolér, LoRaWAN, LoRa, budič LED, světelný zdroj

Překlad názvu: HW řešení systému pro navigaci uvnitř budov s využitím komunikace ve viditelném světle

Contents

1 Introduction	1
2 Theory	3
2.1 Modulation methods	3
2.1.1 OOK - On-Off keying	4
2.1.2 Pulse modulation methods	6
2.1.3 OFDM - Orthogonal Frequency Division Multiplexing	10
2.2 VLC-Based-IPSSs	11
2.2.1 Conventional positioning methods	11
2.2.2 Sensor assisted methods and positioning optimization methods	16
3 Light source design	17
3.1 LoRa shield	17
3.2 Microcontroller	18
3.3 Power source	18
3.4 LED driver circuit	18
3.4.1 Analog Switch IC	18
3.4.2 Power management	20
3.4.3 Voltage to current converter	21
3.4.4 Heat sink	22
3.4.5 Electrical simulations and measurements	24
3.4.6 Temperature measurement	28
4 System testing	31
5 Conclusion and future work	37
A Bibliography	39
B 3W prototype	45
C LoRaWAN ABP communication	47

Figures

<p>2.1 An example of UPSOOK patterns. Adopted from [2]. 4</p> <p>2.2 OOK NZR and RZ (Return-to-Zero waveforms). Adopted from [3]. 5</p> <p>2.3 PWM signal for two different dimming factors, showing difference between PWM period T_{PWM} and on time T_1. Adopted from [4]. 7</p> <p>2.4 Various PWM modulated LEDs captured by CMOS sensor. Adopted from [5]. 7</p> <p>2.5 DMT PWM transmitter block diagram. Adopted from [6]. 8</p> <p>2.6 PWM-sampled DMT signal. Adopted from [4]. 8</p> <p>2.7 Comparison of Pulse Width Modulation (PWM), Pulse Position Modulation (PPM), Variable Pulse Position Modulation (VPPM), Overlapping Pulse Position Modulation (OPPM) and Multipulse Pulse Position Modulation (MPPM). Adopted from [6]. 9</p> <p>2.8 PPM based modulation schemes with Q time slots, N levels and K pulses per symbol. Adopted from [7]. 10</p> <p>2.9 Classification of positioning methods. Adopted from [8]. 12</p> <p>2.10 Conventional positioning algorithms. Adopted from [9]. 12</p> <p>3.1 A block diagram showing proposed VLC transmitter. 17</p> <p>3.2 LED driver schematic from Eagle PCB design software. 19</p> <p>3.3 SPDT switch block diagram for logic 1. Adopted from [10]. 19</p> <p>3.4 TC962EPA application in design. 20</p> <p>3.5 Circuit schematic of the LED driver. 21</p> <p>3.6 The LED driver schematic from OrCAD Capture simulation software. 24</p>	<p>3.7 A conversion of a sinusoidal voltage signal into a current driving the high power LED. The input signal [V] (the blue signal), the output signal of the op-amp [V] (the red wave) and the current through the LED [A] (the green line), temperature [°C] 25</p> <p>3.8 A conversion of a PWM voltage signals into a current driving the high power LED. The input signal [V] (the blue signal), the output signal of the op-amp [V] (the red wave) and the current through the LED [A] (the green line), temperature [°C] 26</p> <p>3.9 10W LED driver prototype with the Nucleo microcontroller. 27</p> <p>3.10 A conversion of a sinusoidal voltage signal into a current driving the high power LED - measured. The green line is a voltage signal on a 1 Ohm resistor, therefore current through the LED [mA]. The yellow signal is the output of the op-amp [V]. 27</p> <p>3.11 A conversion of a PWM voltage signals into a current driving the high power LED measured on an oscilloscope. The green line is a voltage signal on a 1 Ohm resistor, therefore current through the LED [mA]. The yellow signal is the output of the op-amp [V]. 28</p> <p>3.12 A frequency analysis of the voltage to current conversion. The green line is a voltage signal on a 1 Ohm resistor, therefore current through the LED [A]. The red line is the current through the LED [A]. Temperature [°C]. 29</p>
---	--

Tables

3.13 A conversion of a PWM(a) and a sinusoidal(b) voltage signal into a current driving the high power LED measured on an oscilloscope. The green line is a voltage signal on a 1 Ohm resistor, therefore current through the LED [mA]. The yellow signal is the output of the op-amp [V].	29
3.14 Temperature measurements of the LED (a) and the n-mos transistor (b) before a heat sink installment.	30
3.15 Temperature measurements of the LED (a) and the n-mos transistor (b) after the heat sink installment.	30
4.1 10 LED driver PCB design.	31
4.2 Light source system connected to a computer.	32
4.3 Signal measurements on the LED driver extension board. Signals generated by the microcontroller (green wave) [V] and the voltage signal on the 1 Ohm resistor (yellow line) [V], which is equal to current through the LED [A].	34
4.4 LoRa communication testing.	35
B.1 3W LED simulation schematic.	45
B.2 3W LED driver simulation. The yellow wave is the current flowing through the LED [A], the red line is the input voltage signal after the voltage divider [V]. The blue wave is the input signal from the signal generator (sinusoidal signal with 100 Hz frequency, 1.65 V amplitude and 1.65 V DC offset) [V] and the green wave is the output signal of the op-amp [V].	46
B.3 3W LED prototype.	46
3.1 Truth Table for the ADG819. Adopted from [10].	20

List of Listings

4.1	100 Hz sine wave generator.	31
4.2	50 Hz rectangle wave genera- tor.	32
	Code/LoRaWANABP.ino . . .	47



Chapter 1

Introduction

Due to the high demand for an accurate and consistent indoor navigation system, science facilities all over the world keep researching the subject. With the rapid development of satellite-based positioning systems such as the global positioning system (GPS), which had success in outdoor navigation environments [11], a need for indoor positioning systems (IPSs) developed. Such systems offer tracking services, which could be used in a large variety of areas such as robotics, surveillance, indoor parking, indoor location-based services (LBS) etc. Unfortunately, GPS shows poor results both in accuracy and robustness, when it comes to indoor applications. GPS signals (i.e., radio frequency (RF) signals) have low building walls penetration, which leads to a positioning error and therefore can not be deployed in underground environments. [9]

In a search for a high-precision IPS, methods using various technologies were presented. For example technologies using ultrasound [12], radio waves [13], radio-frequency identification (RFID), wireless local area network (WLAN) [14], Bluetooth [15], ZigBee or ultra-wideband (UWB). [16]

Ultrasound indoor positioning algorithms are heavily temperature dependent [17] and therefore have a high positioning error (range of 10 cm)[9]. Techniques using radio frequency signals cause electromagnetic (EM) radiation and thus can not be used in EM sensitive environments (i.e. hospitals, etc.). Other problems that RF IPSs face is a multipath effect caused by the surroundings or dielectric properties of a building, which can cause positioning error up to 0.5 m[18]. Moreover, the radio spectrum is highly congested and protected. WLAN based applications have overall a poor positioning result (around 2 meters [14]) due to its fluctuations in signal sources. Bluetooth and Zigbee face similar issues and have similar positioning errors (Bluetooth average 2 m [19], ZigBee average 1 m [20]). UWB is commonly combined with other technologies, for example, GPS and reaches an accuracy higher than 20 cm, however, it remains highly influenced by the area setting and multipath effect.

A Different solution from traditional techniques presented is represented by visible light communication (VLC) positioning systems. IPSs based on VLC can be divided into two branches: photodiode-based and image-sensor based [5]. Photodiode-based systems are commonly combined with received signal

strength (RSS) algorithms, which determines the position from a comparison of the intensity of multiple received signals. Such systems often cost less but are not stable and robust [21]. This topic is discussed in the next chapter. IS-based (image-sensor based) systems have generally a better performance than PD-based (photodiode-based) systems. Scientists from China have shown in [22] that IS-based systems can also achieve high accuracy for a receiver moving at high speed.

Motivated by the enduring development of VLC positioning systems, this paper presents hardware for a testing environment for any of the mentioned modes IS or PD based and for testing a variety of different algorithms, which are also discussed. This light source communicates with a central unit via LoRa network and works as an IoT system, which simplifies workflow for debugging any positioning algorithm.

This paper is organized as follows: In chapter 2, algorithms and modulation methods for VLC positioning systems are illustrated. In chapter 3, the hardware design for an end node device is presented. In chapter 4, the device and LoRa network is tested and its validity verified in laboratory conditions. Finally, in chapter 5 achieved results are determined.

Chapter 2

Theory

When designing VLC-Based IPS, two essential decisions must be made: which signal modulation method and positioning technique are the most convenient for the assigned use case. A survey of modulations and positioning methods presenting numerous positioning technologies was made to introduce current challenges in the field.

2.1 Modulation methods

There are two important factors when selecting a proper modulation method for VLC-Based IPS: dimming control and flicker control. VLC modulations provide two important functions: data transfer and illumination. Dimming can control the illumination, whilst flicker control can regulate fluctuations of the light intensity, which is crucial for the human eye so that the positioning system does not harm our eyesight. High fluctuations of the light intensity can cause damage to our eyes, hence the amplitude and phase modulations are not suitable for VLC. Both of these functions affect the final data rate. [9]

Paper [6] states that relation between measured and perceived light is non-linear, which means, in other words, that pupil regulates, how much light enters the eye. The perceived light can be calculated as

$$\text{Perceived light}[\%] = 100 \cdot \sqrt{\frac{\text{Measured light}[\%]}{100}}. \quad (2.1)$$

This is essential because in VLC, depending on the application, the user may choose the level of dimming, but the communication should stay unaffected. IEEE 802.15.7 standard [23] advises that flickering should be faster than 200 Hz to prevent any eyesight damage. For obvious reasons modulation schemes must alleviate changes of the light intensity otherwise, they are not applicable in the commercial sphere.

Four types of modulation methods are used for VLC communication. On-Off Keying (OOK), Pulse modulations, Orthogonal Frequency Division Multiplexing (OFDM) and Color Shift Modulation (CSK). CSK uses the intensity of red, green and blue colours to modulate the signal. To achieve

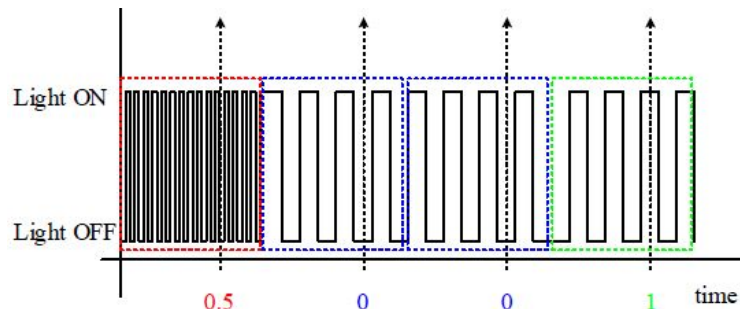
such modulation, RGB LEDs must be deployed. Hardware proposed in this paper does not support CSK modulation and therefore CSK will not be further discussed.

2.1.1 OOK - On-Off keying

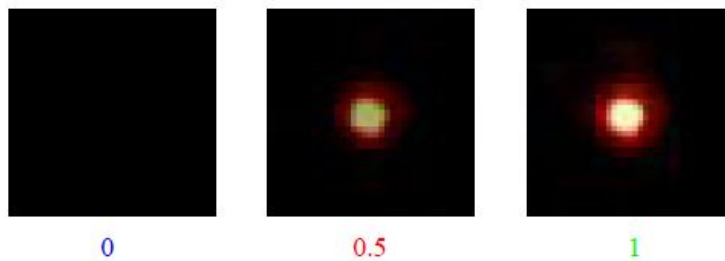
OOK denotes the simplest modulating scheme for digital data transfer. By turning LED on and off we simply transmit data bits 1 and 0. This technique is very easily implemented and thus is widely used for wireless communications. On the other hand, this technique neither allows dimming control nor can not transfer a large amount of data [8]. In VLC the rectangular carrier is most preferred for its minimum fluctuation of light intensity.

OOK can be combined with different modulating techniques. In [2] researchers propose an under-sampled phase shift ON-OFF keying modulation (UPSOOK). An experiment proved that under given conditions this system can reach 150 bps error-free communications for a range of up to 12 m.

In Figure 2.1 we can see a representation of transmitted signal using UPSOOK modulation. Logical 0 and 1 are samples of a rectangle wave that have the same frequency $f_0 = f_1 = n \cdot x$, where $x = f_{camera}$ [FPS] and n is an even number, but different phase shift. Logical 0.5 represents the frame header (FH), which determines the beginning of the data transfer. Generally, a frequency of the FH must be higher than a camera's maximum frame rate (for example 25 kHz).



(a) : Sampled result of a transmitted signal using UPSOOK modulation.



(b) : Three possible sampled results.

Figure 2.1: An example of UPSOOK patterns. Adopted from [2].

A different approach is represented by NRZ(Non-Return-to-Zero) OOK.

LED in Logical 0 state is not completely turned off but the intensity is reduced (see Figure 2.2).

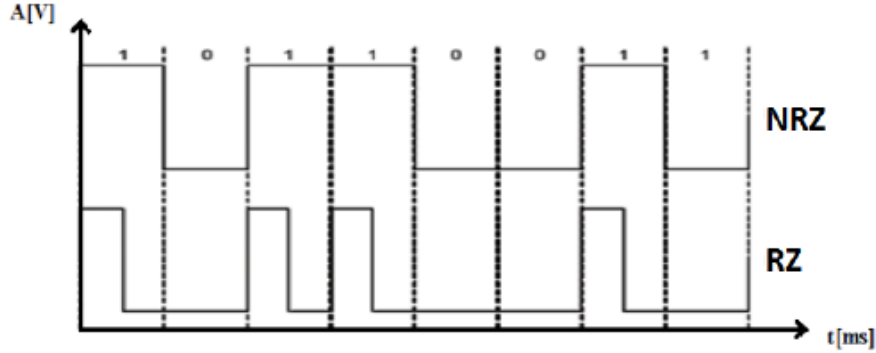


Figure 2.2: OOK NRZ and RZ (Return-to-Zero waveforms). Adopted from [3].

The highest data rate achieved using NRZ-OOK and white LED was shown to be 230 Mbps. New researches focus on using white RGB LEDs and NRZ-OOK modulation for data transfer. System modulating red LED with NRZ-OOK and the two others providing constant current for illumination achieved a data transfer of 477 Mbps. [6]

IEEE 802.15.7 suggests two practices to provide dimming support for the OOK modulation method: controlling ON and OFF levels and compensation periods.

Controlling or redefining ON and OFF levels means changing light intensities for 1s and 0s. Utilizing this practice user achieves a required level of dimming without any communication disruption. Lowering the intensity also decreases communication distance. The major issue might represent a lower driving current for LEDs. LEDs tend to change emitted colour when driving current decreases. [6]

The second solution to dimming control offer so called compensation periods. The ON/OFF levels remain the same, but additional periods are added, when the LED is turned ON and OFF (ON and OFF periods). The period duration is dependent on the requested dimming level. ON periods are added, when necessary level of dimming should be higher than 50% and OFF periods, when otherwise. We can calculate the percentage time of active data transmission (γ) within transmission interval T to secure a dimming level D as

$$\gamma = \begin{cases} (2 - 2D) \cdot 100, & \text{if } D > 0.5 \\ 2D \cdot 100, & \text{if } D \leq 0.5 \end{cases}, \quad (2.2)$$

as shown in [6]. Communication efficiency E_D can be then calculated as

$$E_D = -D \log_2 D - (1 - D) \log_2 (1 - D). \quad (2.3)$$

We can see that the maximum efficiency at dimming is 50%. The disadvantage of this procedure is a reduction in the data rate. However, compensation periods do not influence the communication distance. Inverse source coding

is proposed to solve the lowered data rate and achieving desired dimming control.[6]

■ 2.1.2 Pulse modulation methods

As was already presented, OOK can provide wireless communication services with simple implementation, but with issues regarding data rate and dimming control. Solution present pulse width and position modulation schemes, which will be described next.

■ PWM - Pulse Width Modulation

In PWM pulse width and signal frequency are adjusted. During the pulse, the LED operates at maximum brightness i.e. maximum current flows through the device. The desired level of dimming is achieved through the width of the pulses, while the pulses carry the modulated signal in form of a rectangle wave. Mathematically PWM signal $p(t)$ with period T_{PWM} and for $0 \leq t \leq T_{PWM}$ can be described as

$$p(t) = \begin{cases} 1, & \text{if } 0 \leq t \leq T_1 \\ 0, & \text{if } T_1 < t \leq T_{PWM}. \end{cases} \quad (2.4)$$

In PWM, term of a duty cycle is usually used to describe the signal. It is a fraction of one period in which the signal is active. For duty cycle $d = T_1/T_{PWM}$ is the dimming level δ determined as $\delta = 1 - d$. In Figure 2.3 two different PWM signals with $\delta = 80\%$ and $\delta = 20\%$ are illustrated to describe PWM modulation method in closer detail. [4]

In [5] authors use PWM modulation with various duty-ratios (duty cycles) and frequencies to create a LED recognition system that can be used in IS-based systems. The results of their experiment show that roughly 1035 unique LED-IDs can be offered by the PWM method. Using the CMOS sensor with rolling shutter mechanism and image processing algorithms causes images of LEDs with PWM modulation to project bright stripes. The number of the stripes is dependent on the frequency of the PWM modulation and the width of the stripes is related to the duty-ratio of the modulated signal. In Figure 2.4 we can observe various LEDs modulated with PWM but different modulation properties. LEDs (a)-(c) and (d)-(f) have the same frequencies but different duty-ratios. The number of the stripes is same, but the width of the stripes varies.

In [6] we can read that any level of dimming from 0% to 100% can be reached using high-frequency PWM. It is also important that the intensity of pulses is constant in all cases, therefore unlike OOK with different ON/OFF levels, colour shift in LEDs does not occur. However, the basic PWM scheme offers a data rate only up to 4.8 kbps. To achieve a higher data rate, PWM in combination with DMT (Discrete Multitone) was proposed. Ntogari *et al.* in [4] describe a system, where PWM ensures the dimming function of the modulating scheme, while Quadrature Amplitude Modulation (QAM) is

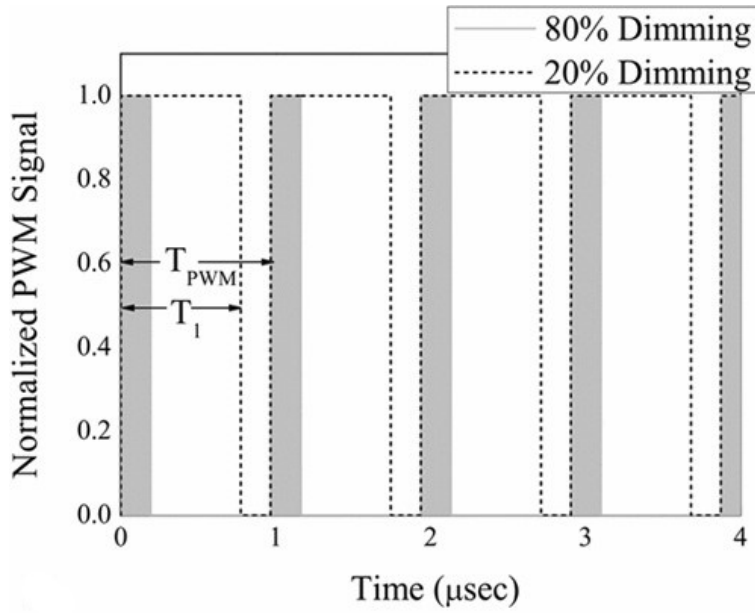


Figure 2.3: PWM signal for two different dimming factors, showing difference between PWM period T_{PWM} and on time T_1 . Adopted from [4].

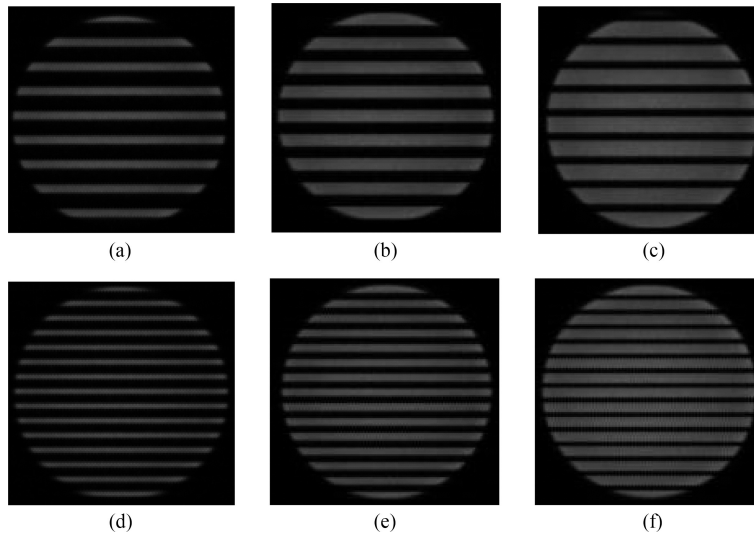


Figure 2.4: Various PWM modulated LEDs captured by CMOS sensor. Adopted from [5].

utilized to map the symbols, which are then transmitted on different DMT subcarriers that are spaced by $1/T$ in frequency, where T is the duration of a single symbol (illustrated in Figure 2.5). Both DMT and PWM signals are combined by multiplication into an output signal, which is then transmitted through the LED. In Figure 2.6 a DMT signal sampled with PWM modulation is presented. Signals from 2.3 are used to sample the same DMT signal.

A data rate of 513 Mbps was achieved using QAM DMT subcarriers, but

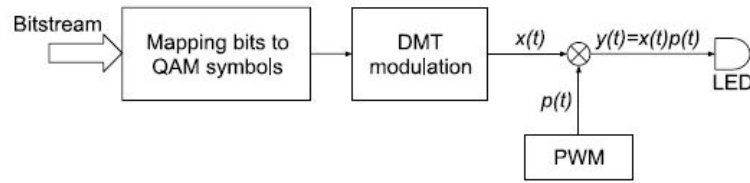


Figure 2.5: DMT PWM transmitter block diagram. Adopted from [6].

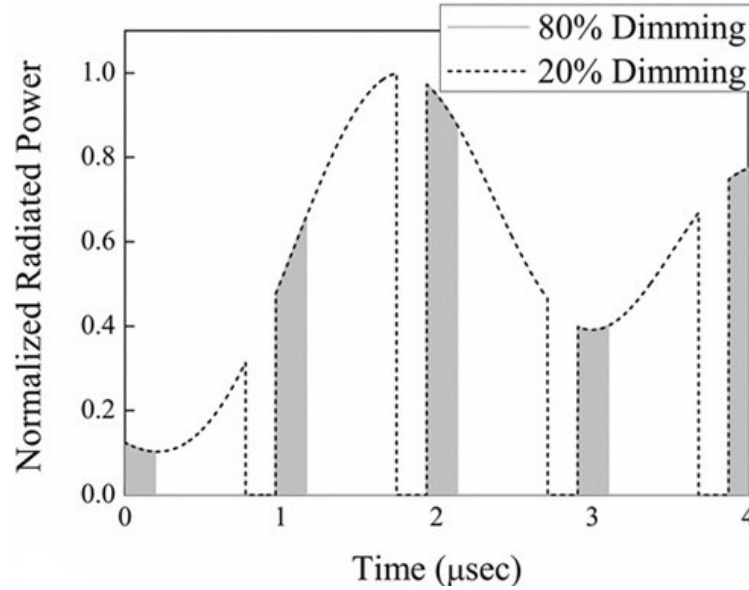


Figure 2.6: PWM-sampled DMT signal. Adopted from [4].

in this particular system, the LED dimming functionality was not addressed properly [6].

■ PPM - Pulse Position Modulation

PPM is a modulation scheme based on the pulse position. The position of the pulse identifies the transmitted symbol. The symbol duration is split into slots of equal duration of t , and the pulse is in one of the slots. For its simplicity, early VLC designs used PPM for wireless communications [8]. However, PPM offers low data rates (only one pulse per symbol duration) and low spectral efficiency.

Due to its disadvantages, other variants of PPM have been proposed. Figure 2.7 demonstrates the difference between PWM and various PPMs.

General improvement to PPM brought Overlapping Pulse Position Modulation (OPPM). OPPM allows different pulse symbols to overlap (see Figure 2.7) and therefore multiple pulses can be transmitted in one symbol duration (continuous pulses). OPPM improves both spectral efficiency and data transfer and also enables better dimming control [6].

Multipulse PPM (MPPM) allows multiple pulses in one symbol duration,

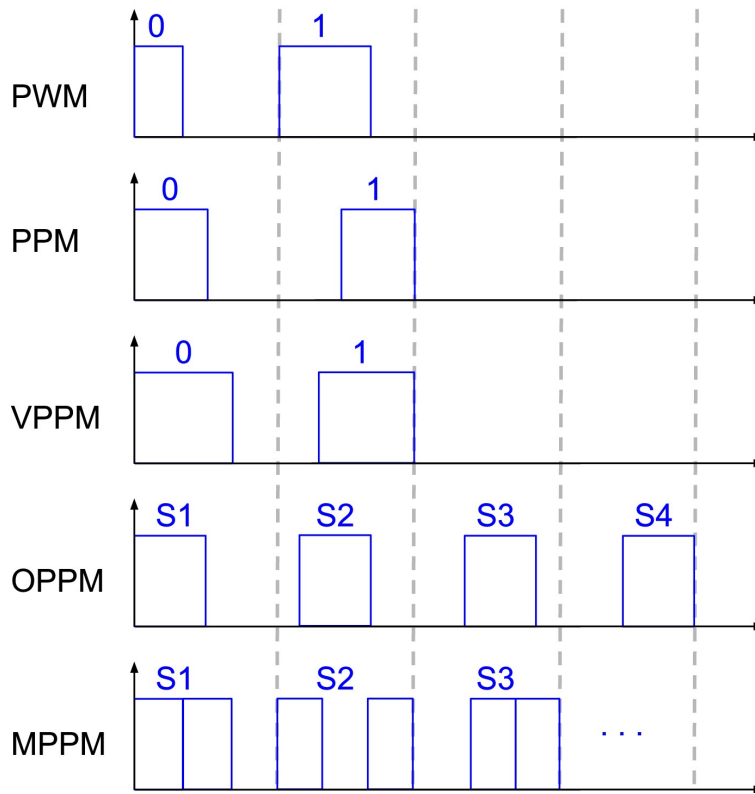


Figure 2.7: Comparison of Pulse Width Modulation (PWM), Pulse Position Modulation (PPM), Variable Pulse Position Modulation (VPPM), Overlapping Pulse Position Modulation (OPPM) and Multipulse Pulse Position Modulation (MPPM). Adopted from [6].

but unlike in OPPM, these pulses do not have to be continuous (illustrated in Figure 2.7). MPPM achieves higher spectral efficiency than OPPM [6].

Variable PPM (VPPM) is a modulation scheme proposed by IEEE 802.15.7 standard [23]. VPPM is a hybrid of PWM and PPM. In VPPM bits are defined by positions in symbol duration as it is in PPM, nonetheless, the width of the pulse can be modified as PWM pulses. This technique offers improved dimming control, whilst retaining the simplicity of PPM (illustrated in Figure 2.7).

Advanced algorithms derived from PPM are Overlapping MPPM (OMPPM), Differential PPM (DPPM), Differential Overlapping PPM (DOPPM), Expurgated PPM (EPPM) and Multilevel EPPM (MEPPM). OMPPM allows multiple pulses in one symbol duration that can overlap as described in [24]. [24] also shows that OMPPM outperforms OOK, PPM, and MPPM in terms of both capacity and cutoff rate for the same bandwidth and the same probability of pulse occurrence. It was also shown that OMPPM with fewer pulse slots and more pulses per symbol duration achieves a better cutoff rate [6].

DPPM is an improvement of PPM. All OFF symbols following a pulse in symbol duration are deleted and the upcoming symbol starts right after the

pulse of the previous symbol. Researches have shown that DPPM average power requirement for a given bandwidth in an optical communication channel has significantly dropped [6].

DOPPM applies differential deletion of OFF symbols to OPPM and through this method a better spectral efficiency and cutoff rate compared to PPM, DPPM and OPPM is achieved [6].

EPPM is a version of MPPM, where the symbols are expurgated to maximize the Hamming distance between symbols (internal symbol distance). EPPM has low spectral efficiency similar to PPM, but can be used to provide dimming support by changing the number of pulses per symbol (K) and the symbol duration (Q) [7]. Figure 2.8 shows the difference between EPPM and related modulation schemes.

Noshad *et al.* proposed in [25] Multilevel EPPM (MEPPM). MEPPM was designed to improve spectral efficiency and increase the constellation size. Symbols are constructed as linear combinations of N EPPM symbols. Flicker-wise MEPPM shows better results than EPPM in mitigating the flicker effect since the presence of multiple intensity levels per symbol causes on average the intensity levels between time slots to change less [7]. Figure 2.8 illustrates MEPPM signal and symbol composition.

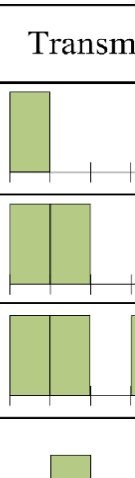
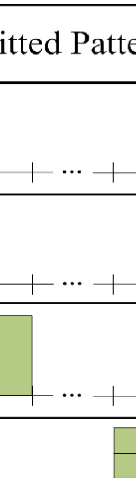
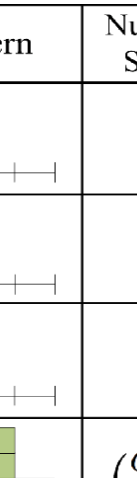
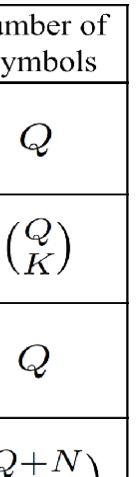
Modulation	Transmitted Pattern	Number of Symbols
PPM		Q
MPPM		$\binom{Q}{K}$
EPPM		Q
MEPPM		$\binom{Q+N}{N}$

Figure 2.8: PPM based modulation schemes with Q time slots, N levels and K pulses per symbol. Adopted from [7].

2.1.3 OFDM - Orthogonal Frequency Division Multiplexing

OFDM is a multi-carrier modulation scheme, which solves problems such as inter-symbol interference and multipath fading. In OFDM, multiple orthogonal subcarriers carry the data in parallel sub-streams. Mostafa *et al.* in [26] proposed VLC OFDM communication and experimentally proved that VLC OFDM can exploit PAR (peak-to-average ratio) that appears in OFDM to intensity modulate LEDs. Nonetheless, VLC OFDM faces multiple chal-

allenges. Firstly OFDM needs to be adapted to VLC communication. IM/DD (intensity-modulation direct-detection) systems such as VLC-based systems, can not comprehend and transmit complex-valued bipolar signals, which are transmitted in RF OFDM. Therefore, Hermitian symmetry constraints must be enforced on the subcarriers to convert complex-valued signals into real-valued and then time-domain signals must be converted into unipolar signals. Depending on the method of conversion from bipolar to unipolar signal, there are two types of OFDM modulation schemes: Asymmetrically-Clipped Optical OFDM (ACO-OFDM) and DC-biased Optical OFDM (DCO-OFDM). [6][9]

ACO-OFDM converts the signal by modulating only odd subcarriers. This procedure leads to symmetric time-domain signal [6]. On the other hand, DCO-OFDM modulates all subcarriers but adds a positive direct current (DC) to convert the signal. The most challenging obstacle in VLC OFDM communication is the non-linearity of current and emitted light in LEDs [6]. The solution in using LED in a small range of currents, where the driving current and optical power are quasi-linear was proposed. Dimming function in OFDM has limited support. However, OFDM presents a large opportunity in VLC communication with data rates up to Gbps [6].

2.2 VLC-Based-IPSS

Conventional positioning techniques, which can be used for VLP (visible light positioning), can be classified into three types: triangulation, proximity and scene analysis (sometimes called fingerprinting). Advanced methods use sensors (image sensors, accelerometers, light sensors etc.) to further achieve better accuracy. Using conventional and sensor-assisted techniques, some accuracy is reached. Nonetheless, there are ways to further improve performance using optimization methods (filtering technique, spring model, normalizing method). [8]

VLP systems can be classified into multiple categories by their complexity and combination of technologies. Figure 2.9 delineates boundaries between VLC-based positioning systems. The main three key-features of every IPS are the mathematical method (meaning conventional method), use of sensors and optimization. This paper will further present a basic overview of the mentioned methods. However, mathematical descriptions of the methods have already been presented for example in [9][8] thus this paper will focus mainly on performance of the methods.

2.2.1 Conventional positioning methods

Figure 2.10 gives us an insight about basic VLC IPSs. This section presents mathematical methods for VLC-based indoor positioning.

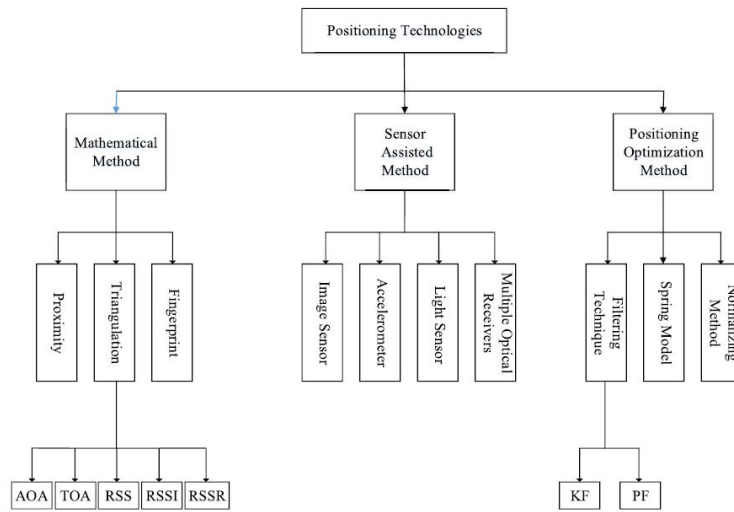


Figure 2.9: Classification of positioning methods. Adopted from [8].

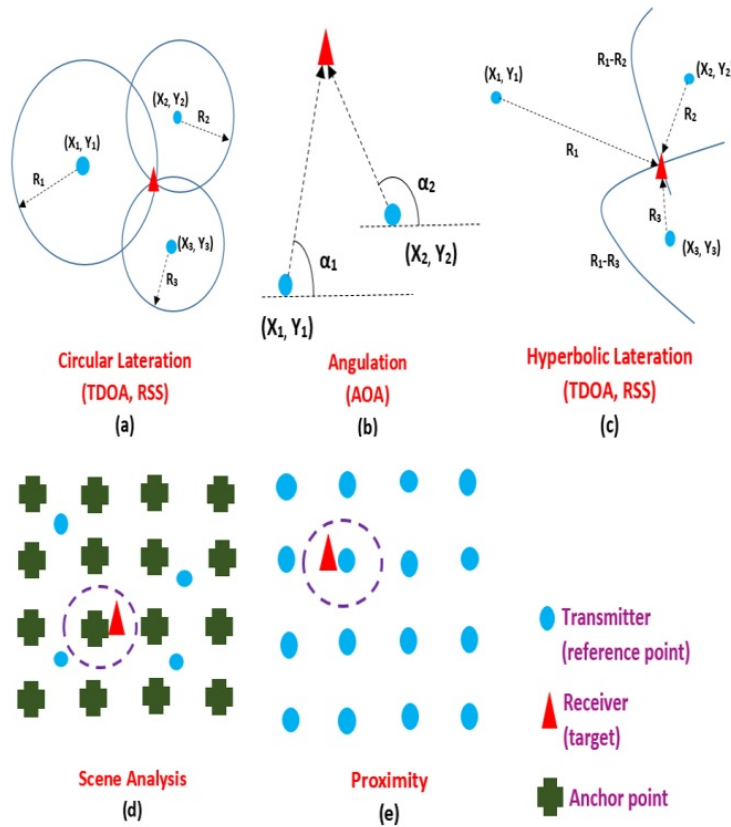


Figure 2.10: Conventional positioning algorithms. Adopted from [9].

■ Triangulation positioning algorithms

VLP systems using triangles and their geometric properties are known as triangulation. Such positioning systems can be further classified into lateration

method and angulation method. The lateration method uses multiple points as reference points (in VLC, light sources) and the position of the target (optical receiver) is derived from the distance between Rx (receiver) and Tx (transmitter - light sources). Lateration methods usually anticipate some distance (distance between LEDs, the height of a room etc.) and the rest is calculated. Techniques used for estimating the position based on lateration method are received signal strength (RSS), time of arrival (TOA), time difference of arrival (TDOA).

Angulation method takes advantage of reference points to evaluate angles between Rx and Tx and the final position can be found as an intersection of multiple light signals. The technique using this method is called the angle of arrival (AOA).

RSS - received signal strength: RSS is an approach that utilizes the intensity of the emitted signal. The signal strength decreases with greater distance, which means that the position can be estimated using signal intensity loss. Scientists utilize these signal path-loss models for IPSSs. It is obvious that these models might fail for several reasons like multipath fading or LED illumination fluctuation [8][21]. However, these problems have been addressed long while ago and methods for improving positioning accuracy have been proposed.

One solution is the application of different signal modulations, for example, OFDM (orthogonal frequency-division multiplexing) as multi-carrier modulation gives better results than IM/DD as a single carrier modulation [8].

A solution of LED illumination fluctuation was proposed in [21] using differential detection positioning algorithm, which utilizes two detectors. An experiment showed that positioning accuracy is improved from 10 cm to 4 cm.

Studies show that there is also a difference in positioning accuracy when using square LEDs and triangle LEDs. Triangle LEDs seem to give better results.[8]

Combining RSS with optimization methods using KF (Kalman Filter) showed promising results and a localization error of 5 cm was achieved. [27]

The most stable and accurate positioning system utilizing RSS was discovered and experimentally tested by Chinese researchers in [28]. This paper focuses on the problem of the tilted receiver angle, and a gyroscope is used to minimize the positioning error. This technique reaches accuracy lower than 1.66 cm in experiments.

TOA - time of arrival: TOA is a method commonly used in GPS. Through precise synchronization between Tx and Rx, a time of travel of a wireless signal is measured and then the distance is estimated. To acquire the precise position of the Rx station, at least three reference points are necessary (three reference points work only in a 2D-plane). Mathematical algorithms utilized for finding the final position is the circular method as shown in Figure 2.10(a) and hyperbolic positioning 2.10(c) [9][8][29]. TOA is for its time synchronization heavily hardware-dependent and therefore only a small amount of research is

focused on this method. IPSs often adopt TDOA instead of TOA to avoid the obligation of precise time synchronization.

A paper dedicated to TOA was presented: [30]. It assumes perfect Tx-Rx synchronization and therefore no experiment was conducted. In the simulation, an accuracy between 2 cm to 5 cm was achieved.

TDOA - time difference of arrival: TDOA is a technique improving TOA. The substantial advantage of TDOA is the need for time synchronization only between base stations and not the target station. Propagation time between Rx and Tx is measured and converted into the distance by multiplication by the speed of the wireless signal in the given environment. The final position of the mobile device is found using the hyperbolic positioning method [29] as shown in Figure 2.10(c). TDOA in comparison with TOA provides a higher positioning accuracy because TOA is heavily affected by the environment [8].

A high precision method was introduced by Korean researchers in [31]. For a space of 5 m x 5m x 3 m, they have reached a positioning error lower than 1 cm. Nonetheless, this was never tested by an experiment and only the simulation is provided.

AOA - angle of arrival: AOA locates the mobile device according to the angle between signals from transmitting stations and the receiver. Using the intersection of multiple signals (illustrated in 2.10(b)) a final position of the target is determined. At least two transmitters are necessary for AOA technique. AOA's advantage is that it does not require any time synchronization.

AOA is in comparison with TOA more sensitive to the external environment, and in theory, TOA should outperform AOA in positioning error. This was never proven in an experiment as was already mentioned in the previous paragraph 2.2.1. Because of AOA's susceptibility to surroundings, positioning accuracy decreases with increasing distance between a mobile device and transmitting stations. This error can be partly corrected by additional hardware, which increases the cost of the system.

Arafa et al. [32] conducted research describing factors, which affect the accuracy of AOA-based IPSs. This paper shows that three main issues are systematic errors, angular precision, and geometry on position uncertainty. The authors also present a comparison of RSS and AOA techniques. Under the same conditions, RSS reaches a four times higher positioning accuracy than the AOA system, which achieved a 5 cm localization error. Unfortunately, this was not proven by experiment.

In [33] researchers show that the AOA method can be used for 3D localization. The simulation shows that the proposed system should reach an accuracy of 0.4 m.

In [34] scientists focus on the integration of angle measuring sensors to calculate the exact location. The experiment proves that this system should reach an accuracy as high as 10 cm.

■ Proximity positioning algorithms

Proximity is the simplest positioning method. It provides relative localization services based on a near transmitter station. Generally, when a mobile device detects a Tx signal, it can presume that the base station is close by. This means that proximity collocates the Rx to the Tx, based on a received signal. If multiple Tx signals arrive at the mobile device, it estimates the location based on the RSS of all signals, because proximity assumes that signal strength is positively related to the distance. As simple as it seems, proximity provides only a rough estimation of Rx position. Based on this, it can be assumed that the positioning accuracy is dependent on the number of transmitters. An issue might occur when multiple signals with the same intensity arrive at the mobile device. Normally we would presume that the target is in the middle of the Txs. [9][8]

In [35] hybrid positioning system combining visible light communication and the ad-hoc wireless network was proposed. The paper presents two designs: one non-carrier and the second 4 MHz carrier VLC positioning techniques. Non-carrier achieves error-free communication in the range 0.33-0.403m. The second carrier technique shows better results. An error-free communication range 0.0057-0.479m is achieved. Both of these methods performed with a minimum positioning error in an indoor obstacle environment with distances of 23.68 m and 77.314 m between an observer and the target.

■ Fingerprinting positioning algorithms

Fingerprinting uses signal analysis for environmentally dependent signals. Fingerprint generally means characteristic or a feature of such signal. In fingerprinting, different features of a signal in different areas are compared and a particular position is estimated [9]. Two fingerprint types are recognized: radio-map based fingerprinting localization and map-free fingerprinting localization [8]. Map-based fingerprint operates in two stages: online and offline stage. Offline stage surveys the indoor environment and generates a radio-map. The localization algorithm uses currently generated radio-map and observed signal strengths to localize the target. As was already mentioned, RSS suffers from multipath effects or illumination fluctuation, which can lead to low positioning accuracy. Map-free techniques use only signal strengths to position the Rx station, therefore, reduce the computing cost of mapping maintaining.

In [36] Yang *et al.* proposed an indoor localization system that uses the signal extinction ratio distribution of LED-based visible light communication. To prevent interference between Txs, the authors proposed sending location code using time-division multiplexing (TDM). The experiment showed a positioning error of 1.5787 cm. In [37] VLC IPS using White-LEDs and the correlation method was presented. In the space of 30 cm x 30 cm x 50 cm, a positioning error of 0.651 cm was achieved.

■ 2.2.2 Sensor assisted methods and positioning optimization methods

To provide the highest positioning precision, IPSs integrate sensors, which assist in reaching a lower localization error. Usually, these sensors are already integrated as part of a device such as a smartphone. The most conventional sensors, which have been widely tested for VLC-Based positioning systems, are image sensor, accelerometer, light sensor and multiple optical receivers (see Figure 2.9). Optimization methods further improve positioning accuracy and trackability. Some examples of such methods are filtering techniques, spring model or the normalizing method. However, these methods are very specific for each IPS, therefore this paper will not further discuss them. More information can be obtained in [9][8] or some examples of high precision methods are [22][38].

Chapter 3

Light source design

This chapter presents a light source design for VLC-Based IPSs and VLC communication. The system proposed in this paper is described in great detail so that any further research in the field can adopt it. Figure 3.1 delineates a block diagram of the light source. The microcontroller and the driver circuit is responsible for digital to analogue data conversion and modulation. The dimming is fully controlled by the user, meaning that the driver circuit is connected to the PWM and DAC outputs of the microcontroller, which can be programmed as desired.

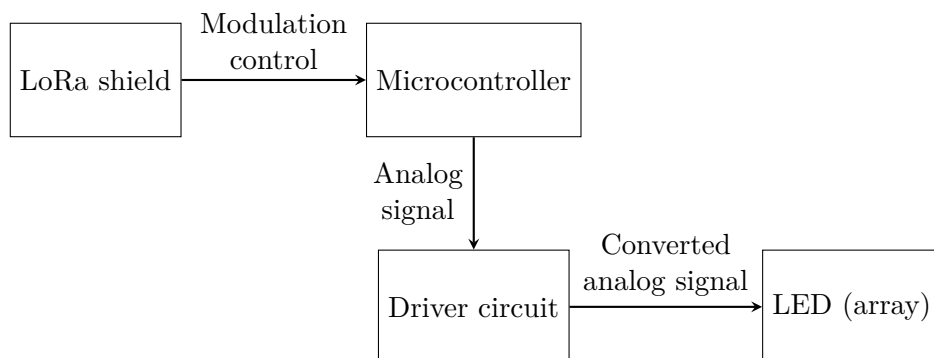


Figure 3.1: A block diagram showing proposed VLC transmitter.

The LoRa shield upon receiving control data from the user forwards these directions to the microcontroller. The microcontroller interprets received data and based on the interpretation, generates an analogue function. This analogue wave then drives current flowing through the LED. The driver circuit converts input voltage from the microcontroller to current flowing through the LED using an operational amplifier (op-amp) and N-channel MOSFET. The proposed system uses a 10 W white LED LEUWU1A301[39].

3.1 LoRa shield

For communication with a LoRa network, a LoRaWAN shield I-NUCLEO-LRWAN1 is used [40]. This expansion board communicates with the microcontroller via a USART communication interface. A wide frequency range

from 860 MHz to 1020 MHz allows deployment of the board in several countries including most of Europe, USA and Australia. Additional specifications can be obtained from [40]. In cooperation with Suda [1], this paper will present software and hardware implementation of the board together with the microcontroller and LED driver.

3.2 Microcontroller

The proposed light source is controlled by STM32 Nucleo board NUCLEO-F446RE [41]. The main reason behind the choice of the board is PWM and DAC programmable outputs and ST Morpho headers, which can be used for additional expansion boards. The board also has a flexible power supply from 7 V to 12 V on the V_{in} pin. This will be used to supply the board from an external power source. The microprocessor can be easily programmed using Arduino IDE in combination with STM32 Cores [42] or Arm Mbed, which simplifies the development process. For additionally information about NUCLEO-F446RE see [41].

3.3 Power source

The external power source is used to power the Nucleo board with the LoRa extension board and the LED driver circuit with the LED. For the means of this design RAC60-24S/OF was selected. It is an AC/DC converter with variable input from 90 V AC to 264 V AC and fixed output 24 V. It also provides 2.5 A maximum output current, which is optimal for the proposed design (more information in subsection 3.4.2). This converter will be connected to the one phase socket of the electric power distribution. For additional information about RAC60-24S/OF see [43].

3.4 LED driver circuit

The LED driver consists of three main parts: input switch integrated circuit (IC), power management block and voltage to current converter, which drives the high power LED. The diver circuit is not only responsible for the LED control, but also for powering the microcontroller and the LoRaWAN extension board. Picture 3.2 shows the whole driver circuit design. Each part of the design is described in the following subsections.

3.4.1 Analog Switch IC

To galvanically isolate PWM and DAC outputs, which are both connected to the same input of the voltage to current converter, a single-pole, double-throw (SPDT) switch is employed, specifically ADG819BRTZ-500RL7 [10]. For illustration figure 3.3(a) presents the application of the switch from Figure 3.2.

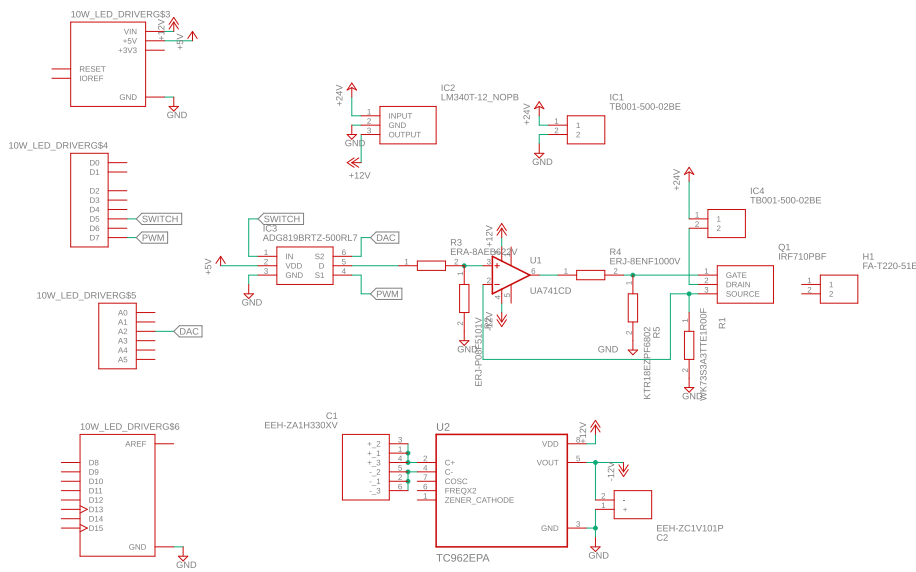
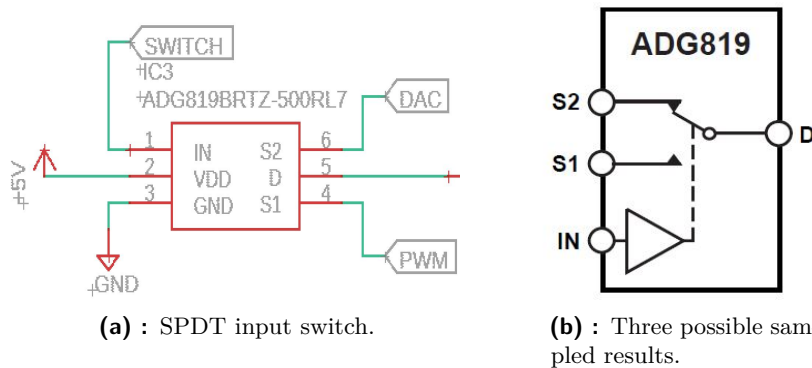


Figure 3.2: LED driver schematic from Eagle PCB design software.



(a) : SPDT input switch.

(b) : Three possible sampled results.

Figure 3.3: SPDT switch block diagram for logic 1. Adopted from [10].

The DAC and PWM signals are output signals from the Nucleo board. The SWITCH signal controls the position of the switch. The D pin of the IC is the output pin. VDD is a power supply pin and GND is the common ground pin. The IC is powered by +5 V output of the board on CN6 pin 5 [41]. The SWITCH signal is a digital output (D5 pin on the board) signal with high and low levels. Figure 3.3(b) illustrates the switching function for logic 1 input.

It may be already clear from Figure 3.3(b), how the switch operates. To make sure everything is well-understood table 3.1 shows the logical function of the switch.

IN	Switch S1	Switch S2
0	ON	OFF
1	OFF	ON

Table 3.1: Truth Table for the ADG819. Adopted from [10].

3.4.2 Power management

As was already mentioned, the driver circuit not only drives the high power LED but also distributes the electrical energy across the device. The whole light source is powered by a +24 V supply voltage. This energy is used to power the Nucleo board and the LoRa extension board, the voltage to current converter, specifically the op-amp used in this device and the LED. The LED represents the highest current draw, which can draw up to 1.5 A [39]. The board draws 250 mA when powered by 12 V [41]. The rest of the system requires low power to function properly and therefore can be neglected.

The +24 V supply is connected using terminal blocks TB001-500-02BE (see Figure 3.2). The +24 V input is connected directly to the LED and N-MOS branch. The LED is connected to the driver using different terminal blocks, therefore, is not in the schematic. To power the board and the op-amp a positive voltage regulator LM340T-12/NOPB [44] and a high current charge pump DC-to-DC converter TC962EPA [45] are used. LM340T-12/NOPB regulates DC voltage from +24 V to +12 V and supplies the Nucleo board and the positive voltage of op-amp. However, the chosen op-amp UA741CD[46] needs to be supplied symmetrically to work properly. TC962EPA is also powered by LM340T-12/NOPB and works as a voltage inverter. TC962EPA requires two external capacitors to provide an inverting function [45]. The selection of properties of these capacitors was based on a measurement from [47], where a typical application and behaviour was shown. Following these guidelines, 33 μ F and 100 μ F capacitors were selected. Figure 3.4 shows the application of TC962EPA. The VDD pin is connected to the +12 V supply provided from LM340T-12/NOPB. The 33 μ F capacitor is connected to the C+ and C- pins according to the capacitor polarity. The 100 μ F capacitor is connected between the VOUT pin and GND with cathode attached to the VOUT pin. A voltage -12 V between VOUT and GND is achieved.

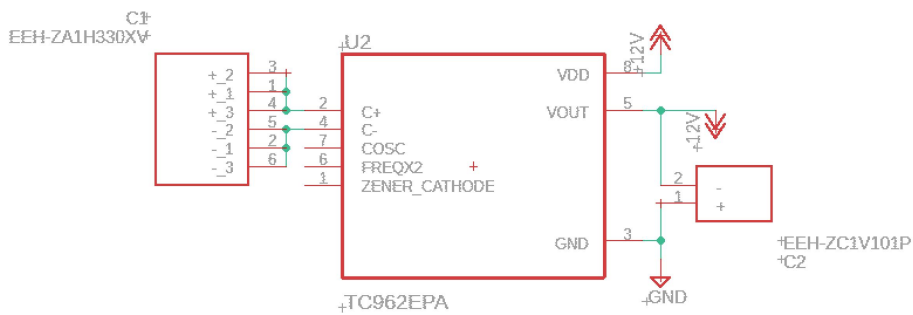


Figure 3.4: TC962EPA application in design.

The proposed supply system does not provide extremely precise voltage values (LM340T-12/NOPB with a voltage output of $12\text{ V} \pm 0.5\text{ V}$ [44], TC962EPA: an exponential behaviour shown in [47]). Nonetheless, this does not present any issues, since the board can be supplied from 9V to 12V and the op-amp output signals do not even remotely reach the $\pm 12\text{ V}$ limit (see subsection 3.4.5).

3.4.3 Voltage to current converter

The main part of the driver is the voltage to current converter. The input voltage signal is converted to a current that flows through the LED, the N-MOS transistor and the resistor. Figure 3.5 describes, how the converter operates.

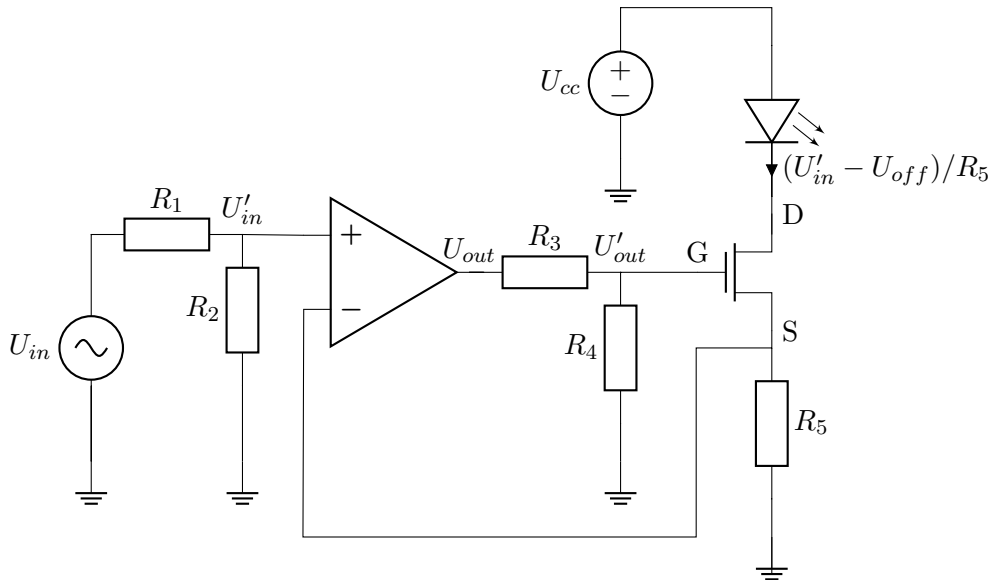


Figure 3.5: Circuit schematic of the LED driver.

The input signal, selected using the SPDT switch (see subsection 3.4.1), must have values between 0 V to 3.3 V. Since negative current cannot flow through the LED, the lowest input value must be 0 V. 3.3 V is the reference value V_{ref} of the microcontroller and the amplitude of the signal can not reach higher values. However, the operational range of the LED is between 0 A and 1.5 A [39], meaning that the input signal must be lowered by more than a half. For this purpose, a voltage divider is used at the input of the converter. In an ideal case, the op-amp will not draw any current. In our case, UA741CD draws maximally 800 nA [46], which can be neglected. Therefore the divider is designed as follows $U_{in} = 0V \dots 3.3V$, $U'_{in} = 0V \dots 1.5V$, meaning that

$$\max\{U'_{in}\} = \max\{U_{in}\} \frac{R_2}{R_2 + R_1}. \quad (3.1)$$

After simple mathematical adjustments we get that

$$\frac{R_2}{R_1} = \frac{\max\{U'_{in}\}}{\max\{U_{in}\} - \max\{U'_{in}\}} = \frac{1.5}{3.3 - 1.5} = \frac{5}{6} \approx \frac{5.1}{6.2}. \quad (3.2)$$

It is obvious that $R_2 = 5.1 \text{ k}\Omega$ and $R_1 = 6.2 \text{ k}\Omega$ resistors will provide the divider function.

The resistors R_3 and R_4 draw away the spare electric charge that is stored in the gate capacitance of the N-MOS transistor. Their values should not affect the output signal U_{out} of the op-amp and therefore $R_3 = 100 \text{ }\Omega$ and $R_4 = 68 \text{ k}\Omega$ were selected. Mathematical description:

$$U'_{out} = U_{out} \frac{R_4}{R_4 + R_3} = U_{out} \frac{68 \text{ k}\Omega}{68 \text{ k}\Omega + 100 \Omega} \doteq 0.999 U_{out} \quad (3.3)$$

In an ideal case U'_{in} would be copied onto R_5 resistor, meaning that $I_{R_5} = U'_{in}/R_5$. However, the input offset voltage of the op-amp is at maximum $U_{off} = 7.5 \text{ mV}$ [46]. This means that

$$I_{R_5} = \frac{U'_{in} - U_{off}}{R_5}. \quad (3.4)$$

If the resistor R_5 is equal to $1 \text{ }\Omega$ then our input voltage signal will be converted into current flowing through R_5 . However, since input bias current of the op-amp is as low as 800 nA , it becomes clear that $I_{R_5} =$ drain-source current $I_{DS} =$ diode current I_D . Substitution of values for $\max\{U_{in}\}$ in 3.4 results in

$$\max\{I_D\} = \frac{\max\{U'_{in}\} - U_{off}}{R_5} = \frac{\max\{U_{in}\} \frac{R_2}{R_2 + R_1} - U_{off}}{R_5} \doteq 1.481 \text{ A}. \quad (3.5)$$

The remaining question is the value of the power supply voltage U_{cc} . To find the correct value we must specify the LED and the N-MOS transistor. The LED we are using LEUWU1A301 has the minimum forward voltage (U_f) 8.9 V and the maximum 10.7 V [39]. The N-MOS used in the design is the IRF710 [48]. Looking at the characteristics of the IRF710 on page 3 of [48], we see that to operate the transistor in the saturation region for a current as high as 1.5 A , at least $U_{DS} = 10 \text{ V}$ (drain-to-source voltage) must be provided. With these values the minimum supply voltage can be determined as $\min\{U_{cc}\} = \max\{U_f\} + \min\{U_{DS}\} + \max\{U'_{in}\} \doteq 10.7 + 10 + 1.5 = 22.2 \text{ V}$. Since this voltage value is difficult to be obtained by any regular power source a 24 V power source was selected.

■ 3.4.4 Heat sink

When using components with large passing currents, a heat sink is necessary to dissipate waste heat. This heat exchanger transfers the heat generated by the component into the surrounding air [49]. Firstly we calculate the maximum power dissipation P_d using the guide from Maxim integrated [50] on the N-MOS. MOSFETs dissipate power due to their drain-source on-state resistance

$R_{DS(on)}$. IRF710 has approximately 3.6Ω when it is in the on state [48]. This power loss P_d is therefore equal to $\max\{I_D\}^2 \cdot R_{DS(on)} \approx 1.5^2 \cdot 3.6 = 8.1 \text{ W}$. However, this is not the only power dissipation in MOSFETs. MOSFET transistors dissipate power as they move through the non-linear region of their VI characteristic meaning that whenever switched on or off, the transistor produces heat. Nonetheless, this dissipation is dependent on the switching frequency of the transistor, which is a changing variable for this design. When choosing the heat sink a reserve for this heat source must be kept.

In Figure 9 of [48], behaviour between the case temperature in $^\circ\text{C}$ and the drain current of the transistor is illustrated. Observation of the behaviour tells us that for I_D is equal to 1.5 A a temperature of the case can not be higher than $75 \text{ }^\circ\text{C}$. Let this value be T_{max} . The temperature of the air is approximately $T_{air} = 25 \text{ }^\circ\text{C}$. Using guidelines from [51] the thermal resistance of the heat sink, which is the deciding factor when selecting a heat sink, can be calculated as follows:

$$R_{th} = \frac{T_{max} - T_a}{P_d} - R_{CS} - R_{JC}, \quad (3.6)$$

where R_{CS} is the case-to-sink thermal resistance (for IRF710 $R_{CS} = 0.5 \text{ }^\circ\text{C/W}$, when mounted directly to the heat sink) and R_{JC} is the junction-to-case thermal resistance (IRF710 maximum $R_{JC} = 3.5 \text{ }^\circ\text{C/W}$). Since it is necessary in this case to use both a mica insulator and a heat sink compound, $R_{CS} = 1.4 \text{ }^\circ\text{C/W}$ was assumed. The maximum R_{JC} is however the worst case. The typical junction-to-case thermal resistance of TO-220 cases is around $1 \text{ }^\circ\text{C/W}$ [51]. Substituting the values in the equation 3.6 results in

$$R_{th} = \frac{75^\circ\text{C} - 25^\circ\text{C}}{8.1\text{W}} - 1.4^\circ\text{C/W} - 1^\circ\text{C/W} \doteq 3.77^\circ\text{C/W}.$$

It is important to follow the same process, to find the heat sink for the LED. The maximum operating temperature of the LEUWU1A301 is $T_{MD} = 135 \text{ }^\circ\text{C}$. In the LED datasheet [39] only R_{CS} is stated. Therefore, the worst scenario $R_{CS} = 2.4 \text{ K/W} = 2.4 \text{ }^\circ\text{C/W}$ is assumed. The mounting of the LED does not require the insulator since the LED is not electrically connected to the heat sink and therefore, only a heat sink compound is used. However, this should not affect the design. The power dissipation of the LED is maximally $P_d = 1.5\text{A} \cdot 10.7\text{V} = 16.05\text{W}$. The necessary thermal resistance of the heat sink for the LED is:

$$R_{th} = \frac{135^\circ\text{C} - 25^\circ\text{C}}{16.05\text{W}} - 2.4^\circ\text{C/W} \doteq 4.45^\circ\text{C/W}.$$

When selecting the heat sink, the thermal resistance should always be lower than the calculated value [51]. Therefore, for the LED the heat sink CHL255A/60 with a thermal resistance $3.6 \text{ }^\circ\text{C/W}$ was selected and for the N-MOS transistor, the MC33266 with a thermal resistance $3.6 \text{ }^\circ\text{C/W}$ [52] was chosen.

3.4.5 Electrical simulations and measurements

Firstly, a simulation of the LED driver circuit was created to verify the function of the system. OrCAD Capture was used as the primer simulator. Figure 3.6 shows the circuit in the software.

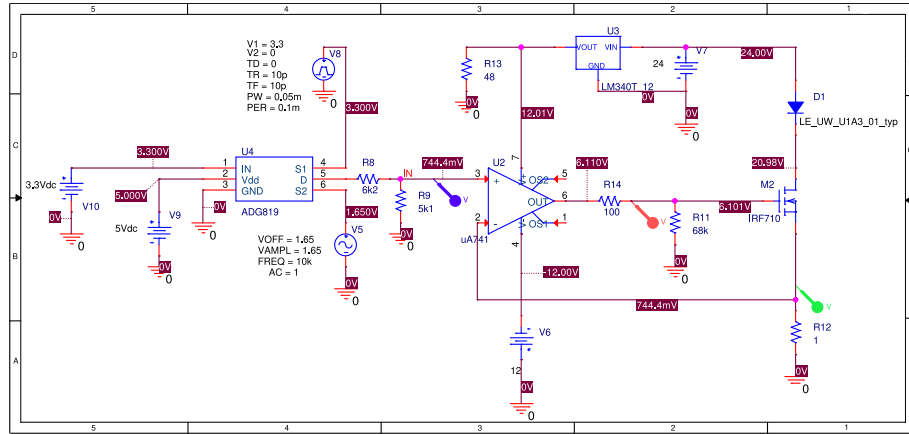


Figure 3.6: The LED driver schematic from OrCAD Capture simulation software.

However, the whole circuit could not be simulated, because the TC962EPA does not have a SPICE model (a simulation model used by the electronic circuit simulator). The source V6 is used to substitute the inverter. The resistor R13 simulates the load of the Nucleo board in the case of a 12 V supply voltage. In the simulation the following signals are tracked: the input signal after the adjustment by the voltage divider (the blue signal), the output signal of the op-amp (the red wave) and the current on the LED (the green signal). The first simulation shows (see Figure 3.7) the conversion of a 10 kHz sinus wave with amplitude 1.65 V and an offset voltage 1.65 V (simulated by the source V5). As shown in Figure 3.7 the V(IN) voltage signal and the I(D1) current are identical.

The second simulation shows a PWM signal with a period 10 ms (a frequency 100 Hz) and a duty-ratio 50 %. The ON level voltage is 3.3 V and the OFF level is 0 V. Figure 3.8(a) shows that the input signal and the driving current are identical. However, the op-amp output voltage drops to -3 V during the OFF level of the PWM. This presents no issue since the transistor minimum gate-source voltage threshold is -20 V. Moreover, as can be seen in the picture, the first OFF-level of the PWM causes the op-amp voltage to drop lower than -6 V. This behaviour is addressed later with the results of the measurement.

The last simulation shows a PWM signal with a 0.1 ms period (a frequency 10 KHz), a duty-ratio 50 % and the same voltage levels as in Figure 3.8(a) (see Figure 3.8(b)). As noticeable, the input voltage signal is not identically converted into the current driving the LED. The rise and fall times of the current are slower than the input voltage rise and fall times.

This is caused by the switching characteristics of the op-amp. As shown in [46] the UA741CD op-amp has slew rate of $0.5 \text{ V}/\mu\text{s}$ and rise time $0.3 \mu\text{s}$. To

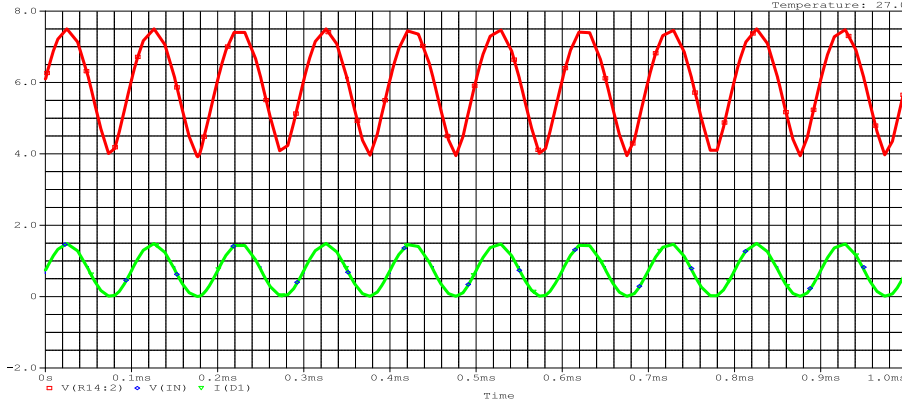


Figure 3.7: A conversion of a sinusoidal voltage signal into a current driving the high power LED. The input signal [V] (the blue signal), the output signal of the op-amp [V] (the red wave) and the current through the LED [A] (the green line), temperature [°C]

properly open the n-mos transistor a highly amplified input signal is required. Using the n-mos data sheet [48] and the simulations, the minimum necessary slew rate for a rectangular wave can be calculated as:

$$\text{slew rate} = \frac{0.9U'_{outPP} - 0.1U'_{outPP}}{t_r}, \quad (3.7)$$

where U'_{outPP} it the peak-to-peak amplitude of the output voltage, which is approximately 3.5 V and t_r is the rise time of the op-amp. Substituting the values results in:

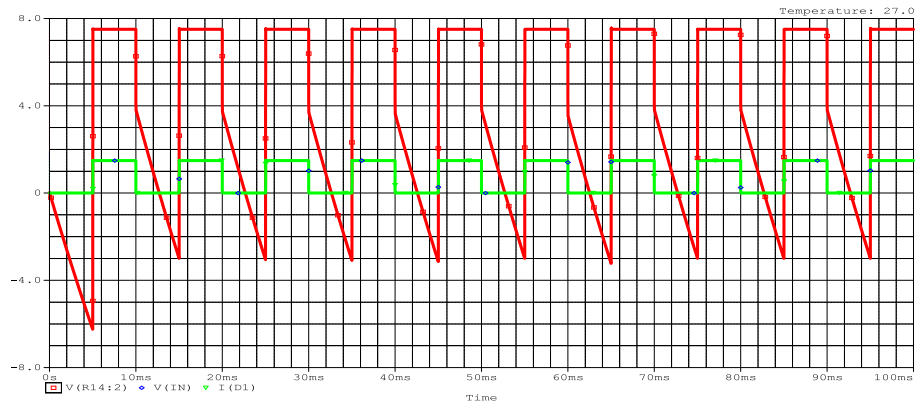
$$\text{slew rate} = \frac{0.9 \cdot 3.5 - 0.1 \cdot 3.5}{0.3 \cdot 10^{-6}} = 9.3V/\mu s.$$

Although the slew rate of the op-amp is lower than the necessary minimum, the signal becomes distorted only, when reaching the frequency threshold of the op-amp, which is around 10 kHz (see Figures 3.8). Additionally a maximum frequency for sinusoidal waves can be calculated as follows:

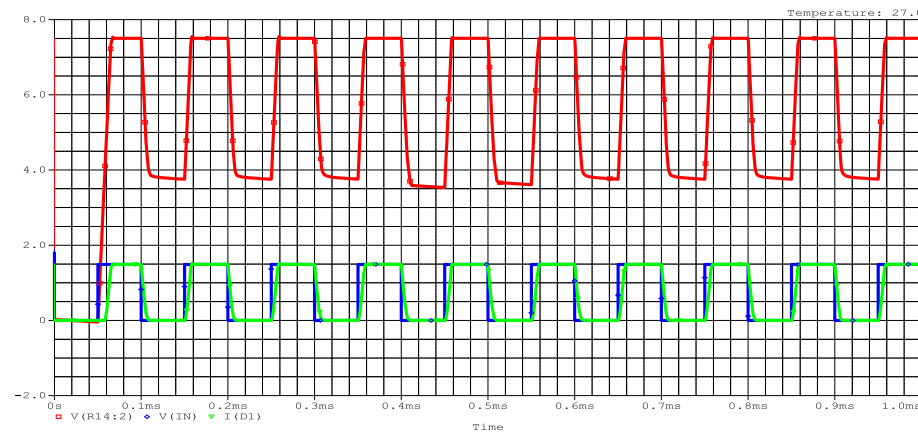
$$f = \frac{\text{slew rate}}{2\pi U'_{outPP}} \approx 23kHz. [53] \quad (3.8)$$

Further this section will present results of the measurements for the simulated signals and a comparison between them. For measuring purposes a prototype of the proposed design was created (see Figure 3.9).

Figure 3.10 presents the measurement of the conversion of the 10 kHz sinusoidal signal from the simulation 3.7. However, the used oscilloscope allows only two signals to be measured at one time. The green wave presents the voltage on the 1 Ohm resistor, and therefore the current driving the LED. The yellow signal is the output signal from the op-amp. It can be seen from the comparison of the measurement and the simulation that the signals correspond and are almost identical.



(a) : 100Hz PWM signal.



(b) : 10kHz PWM signal.

Figure 3.8: A conversion of a PWM voltage signals into a current driving the high power LED. The input signal [V] (the blue signal), the output signal of the op-amp [V] (the red wave) and the current through the LED [A] (the green line), temperature [°C]

Figures 3.11(a) and (b) present measurements of PWM signals 3.8(a) and (b) in the same order. Comparing the measurement 3.11(a) and the simulation 3.8(a) we see that the driving current is almost identical and shows expected behaviour. However, the difference is between the output voltages of the op-amp. The maximum of the measured output voltage of the op-amp is similar to the simulation, however, the minimum is approximately -5.5 V and the behaviour pattern changed from peaks to shifted square waves. This difference can be probably explained by an inaccuracy in the simulation models. Lastly a comparison of 10 kHz PWM signals is presented - the simulation 3.8(b) and the measurement 3.11(b). As is noticeable from both figures, the signals are slightly distorted by the switching characteristics of the op-amp. However, the behaviour of both the simulation and the measurement is similar and the system output is still usable for VLC purposes.

Lastly, Figure 3.12 shows a frequency analysis of the voltage to current conversion. The system is tested from 10 Hz to 100 Mhz and with a 3.3 V

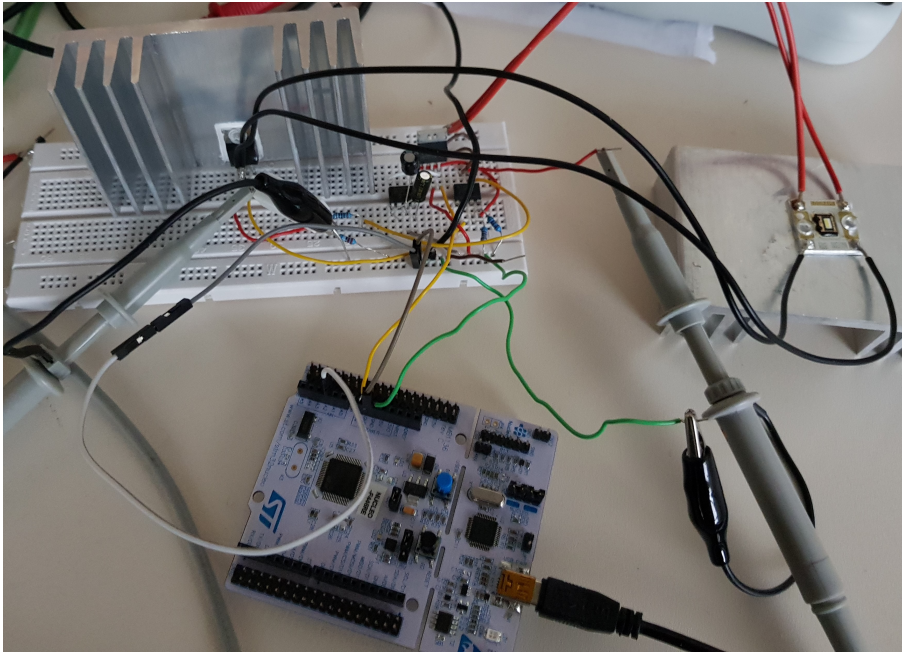


Figure 3.9: 10W LED driver prototype with the Nucleo microcontroller.

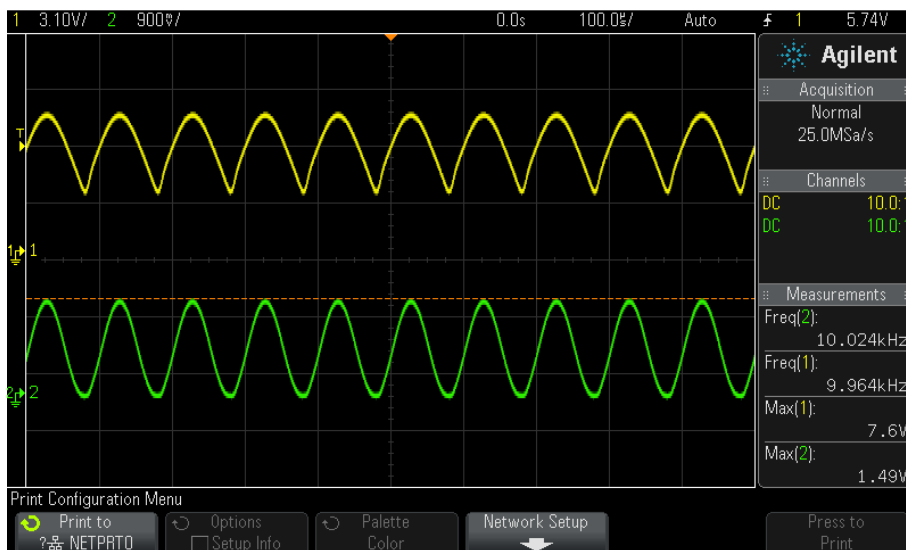
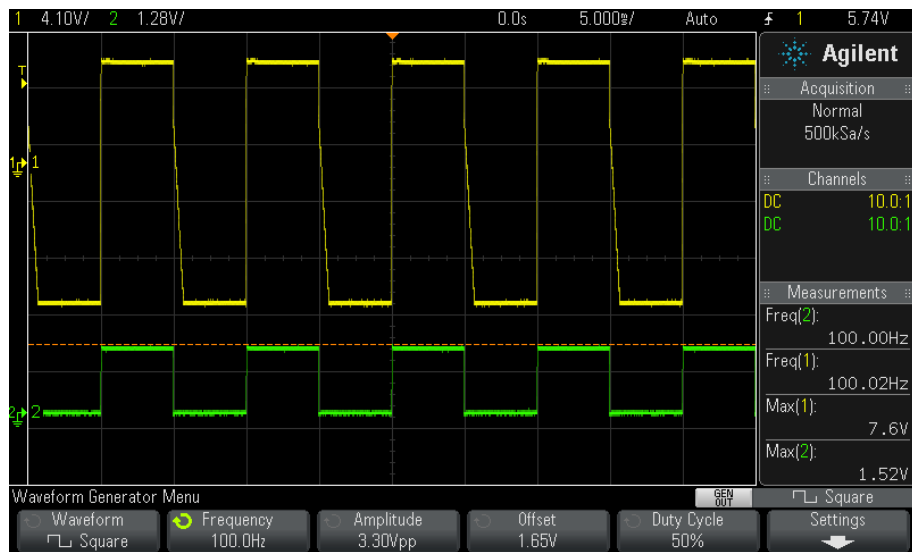
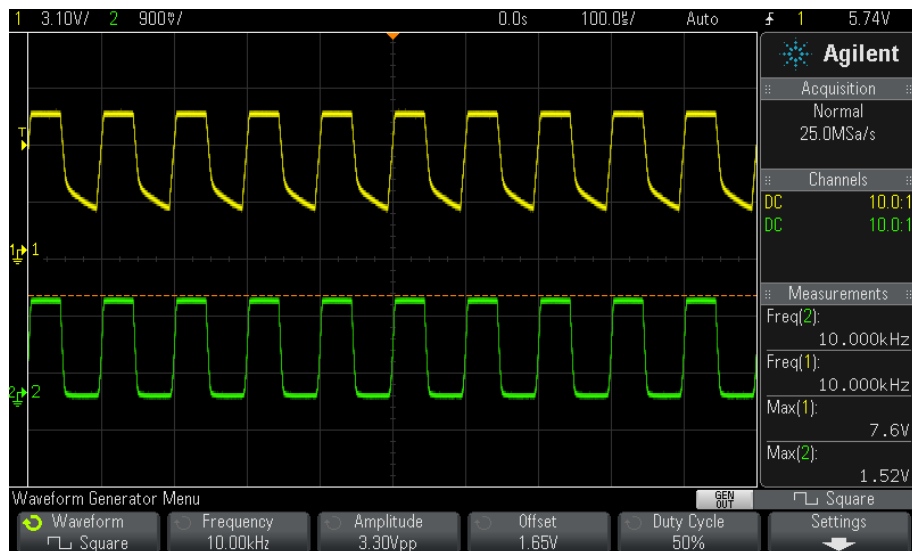


Figure 3.10: A conversion of a sinusoidal voltage signal into a current driving the high power LED - measured. The green line is a voltage signal on a 1 Ohm resistor, therefore current through the LED [mA]. The yellow signal is the output of the op-amp [V].

amplitude. As can be seen from the picture the first noticeable voltage drop starts at 100 kHz, however as was previously explained, the signal will already be highly distorted at frequencies higher than approximately 23 kHz for a sinusoidal signal. The measurements on Figure 3.13 present the level of distortion caused by the insufficient slew rate of the op-amp. Although the



(a) : 100Hz PWM signal - measured.



(b) : 10kHz PWM signal - measured.

Figure 3.11: A conversion of a PWM voltage signals into a current driving the high power LED measured on an oscilloscope. The green line is a voltage signal on a 1 Ohm resistor, therefore current through the LED [mA]. The yellow signal is the output of the op-amp [V].

signals are distorted, the output current still reaches 1.5 A, which is consistent with frequency analysis on Figure 3.12.

3.4.6 Temperature measurement

This subsection presents temperature measurements of the LED and the n-mos transistor following the calculations made in the subsection 3.4.4. The first Figure 3.14 shows the LED and the n-mos transistor with 1 A DC current,

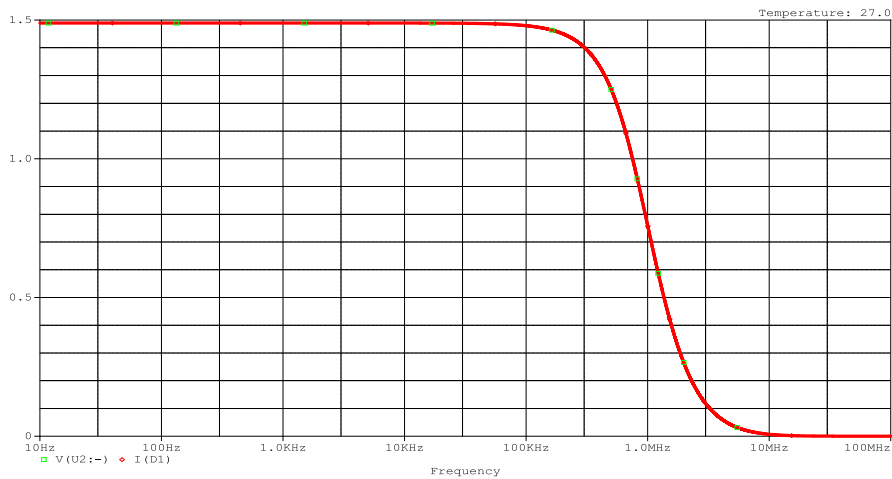
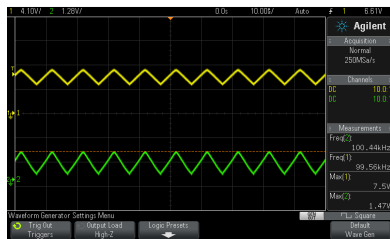
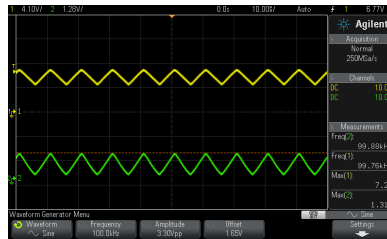


Figure 3.12: A frequency analysis of the voltage to current conversion. The green line is a voltage signal on a 1 Ohm resistor, therefore current through the LED [A]. The red line is the current through the LED [A]. Temperature [°C].



(a) : 100kHz PWM signal - measured.

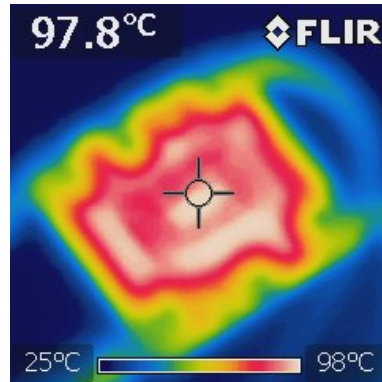


(b) : 100kHz sinusoidal signal - measured.

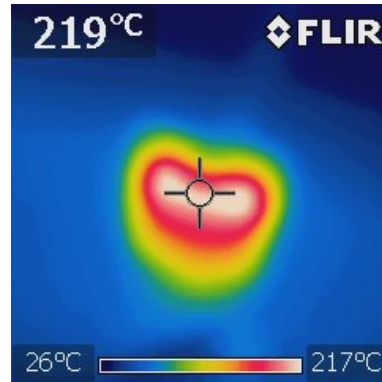
Figure 3.13: A conversion of a PWM(a) and a sinusoidal(b) voltage signal into a current driving the high power LED measured on an oscilloscope. The green line is a voltage signal on a 1 Ohm resistor, therefore current through the LED [mA]. The yellow signal is the output of the op-amp [V].

which is the maximum continuous current that can flow through the LED.

As was predicted the n-mos transistor reaches almost 220 °C, which is above its operating range [48]. The LED reaches almost 98 °C, which is not ideal, but still in the operating range of the device [39]. Figure 3.4.4 shows the temperature measurement of the system after the heat sinks application. The temperature of the LED dropped from approximately 98 °C to 68 °C, which is optimal for any use case. However, the temperature of the n-mos transistor settled on 105 °C, which is still above $T_{max} = 75$ °C, that was set in subsection 3.4.4. Although the temperature is above the maximum value it does not exceed the maximum operating value, which is 150 °C [48] and according to the measurements made in subsection 3.4.5, the signals up to 10 kHz are not disrupted by the transistor’s temperature. For frequencies higher than 10 kHz, the signals might be affected by the insufficient thermal resistance of the heat sink.

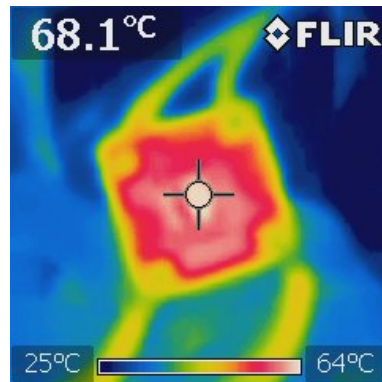


(a) : The LED LEUWU1A301 temperature measurement before a heat sink installation.

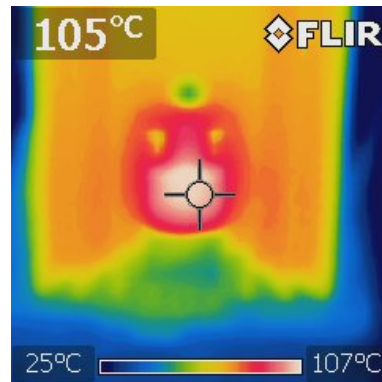


(b) : The n-mos transistor IRF710 temperature measurement before a heat sink installation.

Figure 3.14: Temperature measurements of the LED (a) and the n-mos transistor (b) before a heat sink installment.



(a) : The LED LEUWU1A301 temperature measurement after the heat sink installation.



(b) : The n-mos transistor IRF710 temperature measurement after the heat sink installation.

Figure 3.15: Temperature measurements of the LED (a) and the n-mos transistor (b) after the heat sink installment.

Chapter 4

System testing

Following prototyping and measurements made in the previous chapter, a first version of the LED driver shield was made. This PCB is compatible with ST Morpho headers and therefore is fully controllable by the Nucleo board. However, to make the designed shield compatible with the LoRa extension board a modification had to be made on the LoRa board. To use pin D5 as the switch for ADG819BRTZ-500RL7, the SB28 (0 Ohm connector) had to be removed. This adjustment was based on third party documentation [54], which was accessible in the official ST documentation [40]. Figure 4.1 shows the shield design from Eagle PCB design software, which was manufactured and used in the final prototype (Figure 4.2).

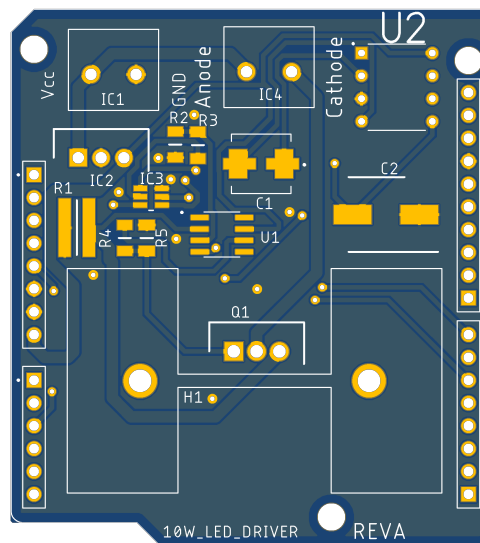


Figure 4.1: 10 LED driver PCB design.

Two types of tests were conducted to test the final prototype. Firstly, a LED modulation test was run to verify the function of the driver. Arm Mbed was used for signal testing purposes. Code 4.1 drives the LED with 100 Hz sinusoidal wave.

```
1 | #include "mbed.h"  
2 | AnalogOut out(A2);  
3 | DigitalOut SWITCH(D5);
```

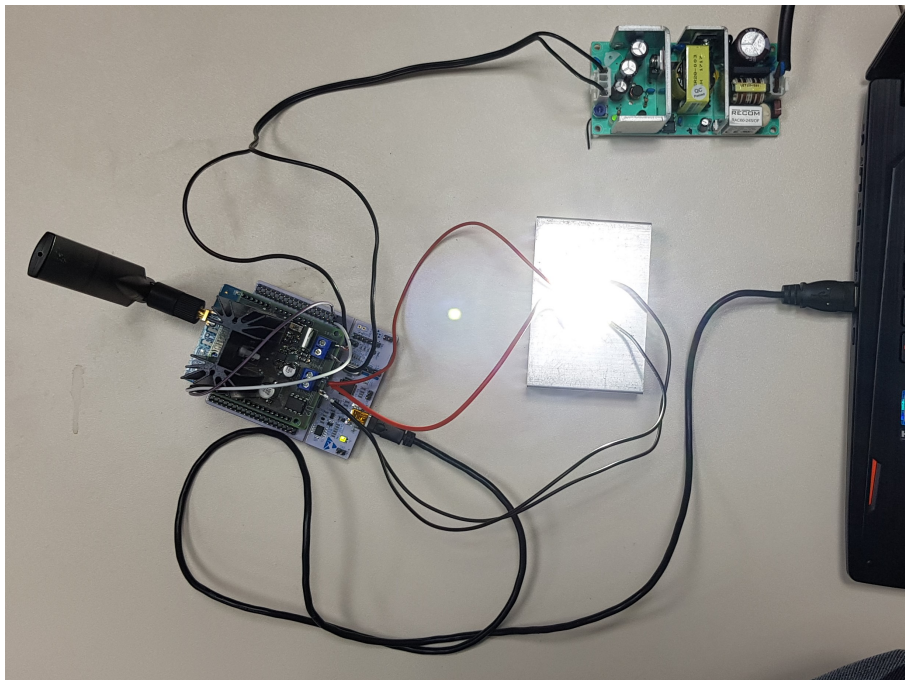


Figure 4.2: Light source system connected to a computer.

```

4  int main() {
5      SWITCH = 1;
6      const float PI = 3.14159265;
7      float A, f, T; // sine peak-to-peak amplitude, frequency
8                      and period
9      float Ts; // sampling time
10     int numberOfPoints = 100;
11     while(1) {
12         SWITCH = 1;
13         A = 1; // amplitude in range 0 to 3.3 V
14         f = 100;
15         T = 1/f;
16         Ts = T / numberOfPoints;
17         for (int i = 0; i < numberOfPoints; i++) {
18             out = 0.5f+(A/2)*sin(2*PI*f*i*Ts);
19             wait(Ts);
20         }
21     }

```

Listing 4.1: 100 Hz sine wave generator.

Code 4.2 drives the LED with 50 Hz PWM signal.

```

1  #include "mbed.h"
2
3  Timeout timer;
4  DigitalOut my_led(LED1);
5  DigitalOut my_pwm(D7); // IO used by pwm_io function
6  DigitalOut SWITCH(D5);
7  int on_delay = 0;

```

```

8 | int off_delay = 0;
9 | void toggleOff(void);
10 |
11 | void toggleOn(void) {
12 |     my_pwm = 1;
13 |     timer.attach_us(toggleOff, on_delay);
14 | }
15 | void toggleOff(void) {
16 |     my_pwm = 0;
17 |     timer.attach_us(toggleOn, off_delay);
18 | }
19 | // p_us = signal period in micro_seconds
20 | // dc   = signal duty-cycle (0.0 to 1.0)
21 | void pwm_io(int p_us, float dc) {
22 |     timer.detach();
23 |     if ((p_us == 0) || (dc == 0)) {
24 |         my_pwm = 0;
25 |         return;
26 |     }
27 |     if (dc >= 1) {
28 |         my_pwm = 1;
29 |         return;
30 |     }
31 |     on_delay = (int)(p_us * dc);
32 |     off_delay = p_us - on_delay;
33 |     toggleOn();
34 | }
35 | int main() {
36 |     SWITCH = 0;
37 |     pwm_io(20000, 0.25); // 20ms - 25%
38 |     while(1) {
39 |         my_led = !my_led;
40 |         wait(0.5);
41 |     }
42 | }

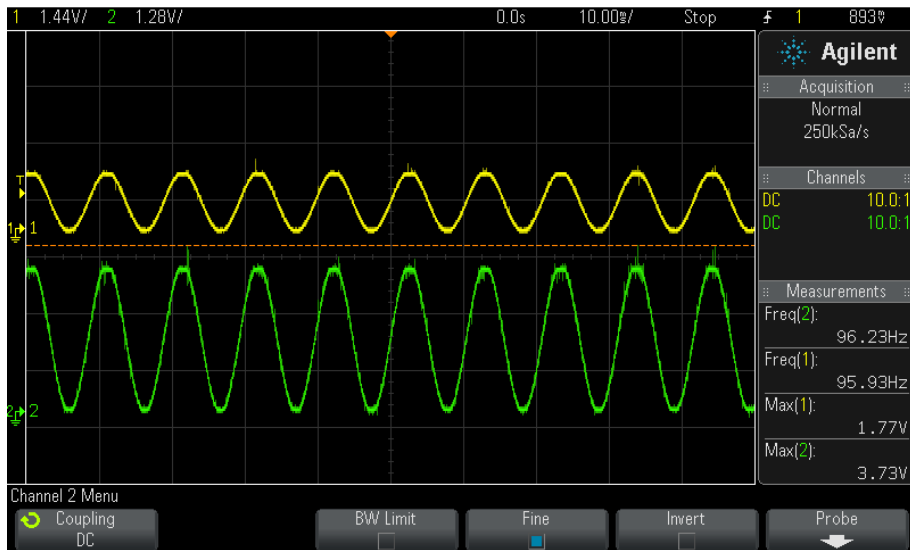
```

Listing 4.2: 50 Hz rectangle wave generator.

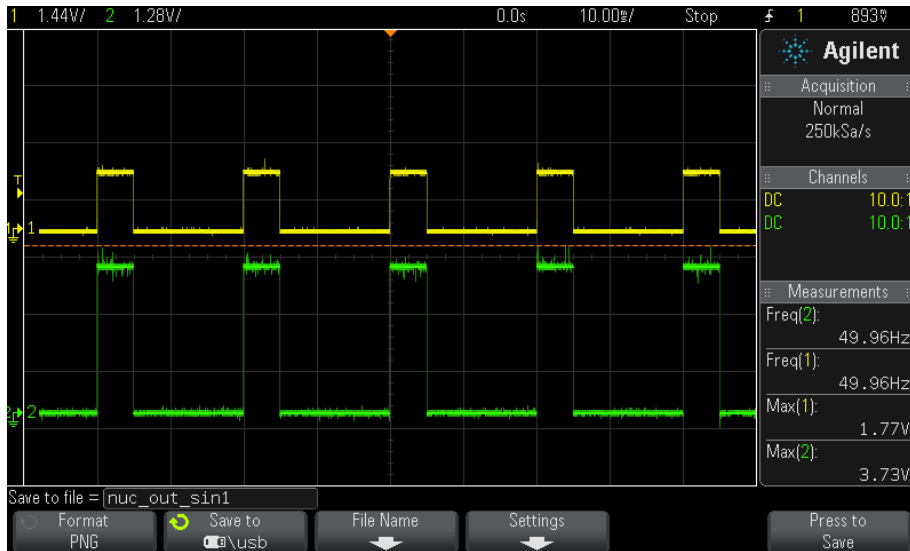
Figure 4.3 shows the measured signals generated by the microcontroller (green wave) and the voltage signal on the 1 Ohm resistor (yellow signal). The measurements show that the conversion of the input signal was undisturbed and proved that the shield connectivity works as predicted.

Lastly Code C tests the LoRa communication with a LoRa gateway. This test was conducted in co-operation with M. Suda [1]. The code is written in Arduino IDE using a library for I-NUCLEO-LRWAN1 accessible at [55]. Library keys.h provides necessary device information that determines the access to the network (for more information see [1]). Code C initiates ABP (Activation By Personalisation [1]) communication and transmits and receives data frames. Collaboration with M. Suda [1] verified the possibility of the communication with LoRa central unit. Figure 4.4(a) presents the messages (uplink) received in the gateway application. The uplink communication worked correctly. Unfortunately, the downlink connection was broken due to an error in the LoRa setting [1]. However, we were able to manually capture

4. System testing



(a) : 100 Hz sinusoidal signal conversion.



(b) : 50 Hz PWM signal conversion.

Figure 4.3: Signal measurements on the LED driver extension board. Signals generated by the microcontroller (green wave) [V] and the voltage signal on the 1 Ohm resistor (yellow line) [V], which is equal to current through the LED [A].

some messages from the gateway. Figure 4.4(b) shows received messages in the node.

12:55:08 PM	uplink
12:54:43 PM	uplink

```

12:54:27 PM      uplink

  applicationID: "1"
  applicationName: "inaviProject-Application"
  deviceName: "seeduino-testNode"
  devEUI: "47db558000360024"
  rxInfo: [ ] 1 item
  0: { } 14 keys
    gatewayID: "b827ebffe061f55"
    time: null
    timeSinceGPSEPOCH: null
    rssi: 3
    loRaSNR: 9.2
    channel: 0
    rfChain: 1
    board: 0
    antenna: 0
    location: { } 5 keys
      latitude: 50.06617519502434
      longitude: 14.302147262431342
      altitude: 0
      source: "UNKNOWN"
      accuracy: 0
      fineTimestampType: "NONE"
      context: "DVgB4w=="
      uplinkID: "1fa5bd1b-0073-451d-917d-a27323d5bbb8"
      crcStatus: "CRC_OK"
    txInfo: { } 3 keys
      frequency: 868100000
      modulation: "LORA"
      loRaModulationInfo: { } 4 keys
        bandwidth: 125
        spreadingFactor: 7
        codeRate: "4/5"
        polarizationInversion: false
      adr: true
      dr: 5
      fCnt: 2
      fPort: 1
      data: "VXBBY2ahAA=="
      objectJSON: "[\"payload\":\"UpAck\"]"
      tags: { } 0 keys
  
```

```

12:58:26.492 -> Online ack sent
12:58:27.642 -> 48 65 6C 6C 6F 2C 20 57 6F 72 6C 64  on port 1
12:58:47.430 -> Online ack sent
12:59:12.218 -> Online ack sent
12:59:36.940 -> Online ack sent
13:00:01.707 -> Online ack sent
13:00:26.448 -> Online ack sent
13:00:51.200 -> Online ack sent
13:01:15.992 -> Online ack sent
13:01:40.732 -> Online ack sent
13:02:05.463 -> Online ack sent
13:02:30.262 -> Online ack sent
13:02:31.449 -> 7B 22 64 75 74 79 43 79 63 6C 65 22 3A 30 2E 35
13:02:51.390 -> Online ack sent
  
```

(a) : Messages received from node in the gateway application. In cooperation with [1].

(b) : Output from the USART communication of the Nucleo board and computer, describing the LoRa network connection based on Code C.

Figure 4.4: LoRa communication testing.



Chapter 5

Conclusion and future work

This paper introduced and explained the main modulation methods used in VLC systems and gave an overview of the important researches that improved knowledge in the field. Furthermore, basic VLC-based navigation algorithms and systems were presented and their performance evaluated by examples of researches.

The focus of the paper was to create hardware for a VLP testbed. The paper presented an idea of how the hardware should work and verified it with simulations, prototypes and measurements. Although the proposed system is not flawless, the issues, which appeared in the development process, were described in detail. Finally, a fully functional light source controlled by a microcontroller NUCLEO-F446RE and with the LoRaWAN connectivity (I-NUCLEO-LRWAN1 extension board) was produced. All the fundamental functions, including the LED (LEUWU1A301) modulation or the LoRaWAN communication, were demonstrated under laboratory conditions. The drafted light source is therefore applicable for testing numerous VLC-based navigation methods.

As far as future work is concerned, improvements on the LED driver, including selecting different op-amp or heat sink with a lower heat resistance should be considered to increase the versatility of the system. Additionally, advanced communication with the LoRaWAN network should be introduced to improve workflow with the testbed. To create a universal testing environment a higher number of the designed light sources must be manufactured.

Appendix A

Bibliography

- [1] M. Suda, “Sw for indoor visible light positioning testbed,” Bachelor’s Thesis, CTU FEE, Technická 2, 5 2020.
- [2] P. Luo, Z. Ghassemlooy, H. Le Minh, X. Tang, and H. Tsai, “Under-sampled phase shift on-off keying for camera communication,” in *2014 Sixth International Conference on Wireless Communications and Signal Processing (WCSP)*, Oct 2014, pp. 1–6.
- [3] L. Andrej, F. Perecar, J. Jaros, M. Papes, P. Koudelka, J. Latal, J. Cubik, and V. Vasinek, “Features and range of the fso by use of the ofdm and qam modulation in different atmospheric conditions,” vol. 9103, 05 2014, p. 910300.
- [4] G. Ntogari, T. Kamalakis, J. Walewski, and T. Spicopoulos, “Combining illumination dimming based on pulse-width modulation with visible-light communications based on discrete multitone,” *IEEE/OSA Journal of Optical Communications and Networking*, vol. 3, no. 1, pp. 56–65, January 2011.
- [5] C. Xie, W. Guan, Y. Wu, L. Fang, and Y. Cai, “The led-id detection and recognition method based on visible light positioning using proximity method,” *IEEE Photonics Journal*, vol. 10, no. 2, pp. 1–16, April 2018.
- [6] P. H. Pathak, X. Feng, P. Hu, and P. Mohapatra, “Visible light communication, networking, and sensing: A survey, potential and challenges,” *IEEE Communications Surveys Tutorials*, vol. 17, no. 4, pp. 2047–2077, Fourthquarter 2015.
- [7] M. Noshad and M. Brandt-Pearce, “Can visible light communications provide gb/s service?” 08 2013.
- [8] J. Luo, L. Fan, and H. Li, “Indoor positioning systems based on visible light communication: State of the art,” *IEEE Communications Surveys Tutorials*, vol. 19, no. 4, pp. 2871–2893, Fourthquarter 2017.
- [9] N. Chaudhary, L. N. Alves, and Z. Ghassemblooy, “Current trends on visible light positioning techniques,” in *2019 2nd West Asian Colloquium*

- on *Optical Wireless Communications (WACOWC)*, April 2019, pp. 100–105.
- [10] A. Devices, “ADG819BRTZ-500RL7,” <https://cz.mouser.com/datasheet/2/609/ADG819-1503098.pdf>, 2012, original product from Analog Devices.
- [11] K. Gligorić, M. Ajmani, D. Vukobratović, and S. Sinanović, “Visible light communications-based indoor positioning via compressed sensing,” *IEEE Communications Letters*, vol. 22, no. 7, pp. 1410–1413, July 2018.
- [12] N. B. Priyantha, A. K. Miu, H. Balakrishnan, and S. Teller, “The cricket compass for context-aware mobile applications,” in *Proceedings of the 7th Annual International Conference on Mobile Computing and Networking*, ser. MobiCom ’01. New York, NY, USA: Association for Computing Machinery, 2001, p. 1–14. [Online]. Available: <https://doi.org/10.1145/381677.381679>
- [13] P. Bahl and V. N. Padmanabhan, “Radar: an in-building rf-based user location and tracking system,” in *Proceedings IEEE INFOCOM 2000. Conference on Computer Communications. Nineteenth Annual Joint Conference of the IEEE Computer and Communications Societies (Cat. No.00CH37064)*, vol. 2, March 2000, pp. 775–784 vol.2.
- [14] Y. Xu, Y. Wang, and L. Ma, “A novel wlan indoor positioning algorithm based on positioning characteristics extraction,” in *2010 Fourth International Conference on Genetic and Evolutionary Computing*, Dec 2010, pp. 134–137.
- [15] J. Nieminen, C. Gomez, M. Isomaki, T. Savolainen, B. Patil, Z. Shelby, M. Xi, and J. Oller, “Networking solutions for connecting bluetooth low energy enabled machines to the internet of things,” *IEEE Network*, vol. 28, no. 6, pp. 83–90, Nov 2014.
- [16] A. Hameed and H. A. Ahmed, “Survey on indoor positioning applications based on different technologies,” in *2018 12th International Conference on Mathematics, Actuarial Science, Computer Science and Statistics (MACS)*, Nov 2018, pp. 1–5.
- [17] C. Hsiao and P. Huang, “Two practical considerations of beacon deployment for ultrasound-based indoor localization systems,” in *2008 IEEE International Conference on Sensor Networks, Ubiquitous, and Trustworthy Computing (sutc 2008)*, June 2008, pp. 306–311.
- [18] H. K. Parikh and W. R. Michalson, “Error mechanisms in an rf-based indoor positioning system,” in *2008 IEEE International Conference on Acoustics, Speech and Signal Processing*, March 2008, pp. 5320–5323.
- [19] S. Yang and B. Wang, “Residual based weighted least square algorithm for bluetooth/uwb indoor localization system,” in *2017 36th Chinese Control Conference (CCC)*, July 2017, pp. 5959–5963.

- [20] Z. Dong, C. Mengjiao, and L. Wenjuan, "Implementation of indoor fingerprint positioning based on zigbee," in *2017 29th Chinese Control And Decision Conference (CCDC)*, May 2017, pp. 2654–2659.
- [21] H. Lv, L. Feng, A. Yang, P. Guo, H. Huang, and S. Chen, "High accuracy vlc indoor positioning system with differential detection," *IEEE Photonics Journal*, vol. 9, pp. 1–13, 06 2017.
- [22] W. Guan, X. Chen, M. Huang, Z. Liu, Y. Wu, and Y. Chen, "High-speed robust dynamic positioning and tracking method based on visual visible light communication using optical flow detection and bayesian forecast," *IEEE Photonics Journal*, vol. 10, no. 3, pp. 1–22, June 2018.
- [23] "IEEE standard for local and metropolitan area networks—part 15.7: Short-range wireless optical communication using visible light," *IEEE Std 802.15.7-2011*, pp. 1–309, Sep. 2011.
- [24] T. Ohtsuki, I. Sasase, and S. Mori, "Overlapping multi-pulse pulse position modulation in optical direct detection channel," in *Proceedings of ICC '93 - IEEE International Conference on Communications*, vol. 2, May 1993, pp. 1123–1127 vol.2.
- [25] M. Noshad and M. Brandt-Pearce, "Multilevel pulse-position modulation based on balanced incomplete block designs," in *2012 IEEE Global Communications Conference (GLOBECOM)*, Dec 2012, pp. 2930–2935.
- [26] M. Z. Afgani, H. Haas, H. Elgala, and D. Knipp, "Visible light communication using ofdm," in *2nd International Conference on Testbeds and Research Infrastructures for the Development of Networks and Communities, 2006. TRIDENTCOM 2006.*, 2006, pp. 6 pp.–134.
- [27] M. Rahaim, G. B. Prince, and T. D. C. Little, "State estimation and motion tracking for spatially diverse vlc networks," in *2012 IEEE Globecom Workshops*, Dec 2012, pp. 1249–1253.
- [28] E. . Jeong, S. . Yang, H. . Kim, and S. . Han, "Tilted receiver angle error compensated indoor positioning system based on visible light communication," *Electronics Letters*, vol. 49, no. 14, pp. 890–892, July 2013.
- [29] R. Kaune, "Accuracy studies for tdoa and toa localization," in *2012 15th International Conference on Information Fusion*, July 2012, pp. 408–415.
- [30] T. Q. Wang, Y. A. Sekercioglu, A. Neild, and J. Armstrong, "Position accuracy of time-of-arrival based ranging using visible light with application in indoor localization systems," *Journal of Lightwave Technology*, vol. 31, no. 20, pp. 3302–3308, Oct 2013.
- [31] S. Jung, S. Hann, and C. Park, "Tdoa-based optical wireless indoor localization using led ceiling lamps," *IEEE Transactions on Consumer Electronics*, vol. 57, no. 4, pp. 1592–1597, November 2011.

- [32] A. Arafa, S. Dalmiya, R. Klukas, and J. Holzman, “Angle-of-arrival reception for optical wireless location technology,” *Optics Express*, vol. 23, 03 2015.
- [33] A. Hajihoseini, A. Dargahi, and A. Ghorashi, “3d indoor localization using visible light communications,” *IJIREEICE*, vol. 4, pp. 119–122, 07 2016.
- [34] X. Liu, H. Makino, and Y. Maeda, “Basic study on indoor location estimation using visible light communication platform,” in *2008 30th Annual International Conference of the IEEE Engineering in Medicine and Biology Society*, Aug 2008, pp. 2377–2380.
- [35] Y. U. Lee and M. Kavehrad, “Two hybrid positioning system design techniques with lighting leds and ad-hoc wireless network,” *IEEE Transactions on Consumer Electronics*, vol. 58, no. 4, pp. 1176–1184, 2012.
- [36] S.-H. Yang, D.-R. Kim, H.-S. Kim, Y.-H. Son, and S.-K. Han, “Visible light based high accuracy indoor localization using the extinction ratio distributions of light signals,” *Microwave and Optical Technology Letters*, vol. 55, no. 6, p. 1385–1389, 2013.
- [37] S. Hann, J. Kim, S. Jung, and C. Park, “White led ceiling lights positioning systems for optical wireless indoor applications,” in *36th European Conference and Exhibition on Optical Communication*, 2010, pp. 1–3.
- [38] S. Yang, E. Jung, and S. Han, “Indoor location estimation based on led visible light communication using multiple optical receivers,” *IEEE Communications Letters*, vol. 17, no. 9, pp. 1834–1837, 2013.
- [39] O. O. S. GmbH., “LE UW U1A3 01,” https://dammedia.osram.info/media/resource/hires/osram-dam-6715835/LE%20UW%20U1A3%2001_EN.pdf, 2018, original document from OSRAM Opto Semiconductors.
- [40] STMicroelectronics, “I-NUCLEO-LRWAN1,” https://www.st.com/resource/en/data_brief/i-nucleo-lrwan1.pdf, 2018, original product from USI® in partnership with STMicroelectronics.
- [41] —, “NUCLEO-F446RE,” https://www.st.com/resource/en/user_manual/dm00105823-stm32-nucleo64-boards-mb1136-stmicroelectronics.pdf, 2019, original product from STMicroelectronics.
- [42] F. Pillon, “stm32duino,” https://github.com/stm32duino/wiki/wiki/Getting-Started?fbclid=IwAR1eQgXe_BLS2R2dTGfv1kA5VkkJEO1PBkI3iHDwc15YPvRgXfviUPrsK4w, 8 2019, (Accessed on 05/05/2020).
- [43] RECOM, “RAC60-24S/OF,” <https://docs.rs-online.com/c25a/0900766b81369a00.pdf>, 2018, original product from RECOM.

- [44] T. Instruments, “LM340T-12/NOPB,” <http://www.ti.com/general/docs/suppproductinfo.tsp?distId=26&gotoUrl=http%3A%2F%2Fwww.ti.com%2Flit%2Fgpn%2Fm340>, 2020, original product from Texas Instruments.
- [45] M. Technology, “TC962EPA,” <https://cz.mouser.com/datasheet/2/268/21484b-74623.pdf>, 2002, original product from Microchip Technology Inc.
- [46] T. Instruments, “UA741CD,” <https://www.gme.cz/data/attachments/dsh.310-515.1.pdf>, 2018, original product from Texas Instruments.
- [47] T. Pulsar, “The pulsar engineering,” <http://www.thepulsar.be/article/tc962/>, 7 2014, (Accessed on 04/03/2020).
- [48] VISHAY, “IRF710,” <https://www.gme.cz/data/attachments/dsh.213-180.1.pdf>, 2011, original product from VISHAY.
- [49] A. A. Components, “Heatsink design and selection - overview,” <http://www.abl-heatsinks.co.uk/heatsink/heatsink-selection-overview.htm>, 2016, (Accessed on 04/06/2020).
- [50] M. Integrated, “Guide to mosfet power dissipation calculation in high-power supply | maxim integrated,” <https://www.maximintegrated.com/en/design/technical-documents/tutorials/1/1832.html>, 10 2002, (Accessed on 04/06/2020).
- [51] R. E. Innovation, “Heatsink calculations – renewable energy innovation,” <https://www.re-innovation.co.uk/docs/heatsink-calculations/>, (Accessed on 04/06/2020).
- [52] MULTICOMP, “MC33266,” <https://datasheet.octopart.com/MC33266-Multicomp-datasheet-13167872.pdf>, 2012, original product from MULTICOMP.
- [53] A. DEVICES, “The op amp,” <https://www.analog.com/media/en/training-seminars/design-handbooks/Basic-Linear-Design/Chapter1.pdf>, (Accessed on 04/24/2020).
- [54] “Github - usiwp1module/usi_i-nucleo-lrwan1,” https://github.com/USIWP1Module/USI_I-NUCLEO-LRWAN1, 2020, (Accessed on 05/08/2020).
- [55] “Github - stm32duino/i-nucleo-lrwan1: Arduino library to support i-nucleo-lrwan1 lora® expansion board based on usi® lorawan™ technology module.” <https://github.com/stm32duino/I-NUCLEO-LRWAN1>, (Accessed on 05/08/2020).
- [56] VISHAY, “IRFD110,” <https://www.gme.cz/data/attachments/dsh.213-059.1.pdf>, 2010, original product from VISHAY.

A. Bibliography

- [57] GETIAN, “GT-P03W54103260,” <https://www.gme.cz/data/attachments/dsh.518-235.1.pdf>, 2015, original product from GETIAN.

Appendix B

3W prototype

The bachelor's project aimed to create a similar LED driver as the LED driver, which was presented in the main part of the paper. However, the goal was to create a driver for 3 W LED. The outcome is illustrated in the following pictures. Figure B.1 shows the schematic of the driver, which is using a UA741 op-amp and IRFD110 [56] transistor. The LED presented in the diagram is different from the LED, which was used in the prototype (GT-P03W54103260 [57]).

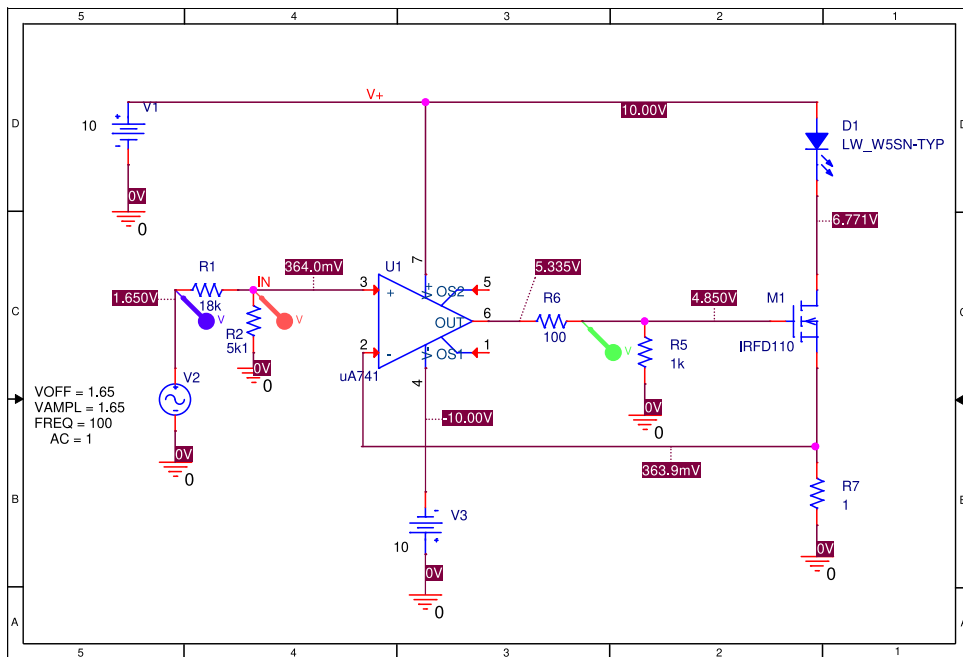


Figure B.1: 3W LED simulation schematic.

Figure B.2 is a simulation of the schematic above. The yellow wave shows the current flowing through the LED and it is identical to the red wave, which is the input voltage signal after the voltage divider. The blue wave is the input signal from the signal generator (sinusoidal signal with 100 Hz frequency, 1.65 V amplitude and 1.65 V DC offset) and the green wave is the output signal of the op-amp.

B. 3W prototype

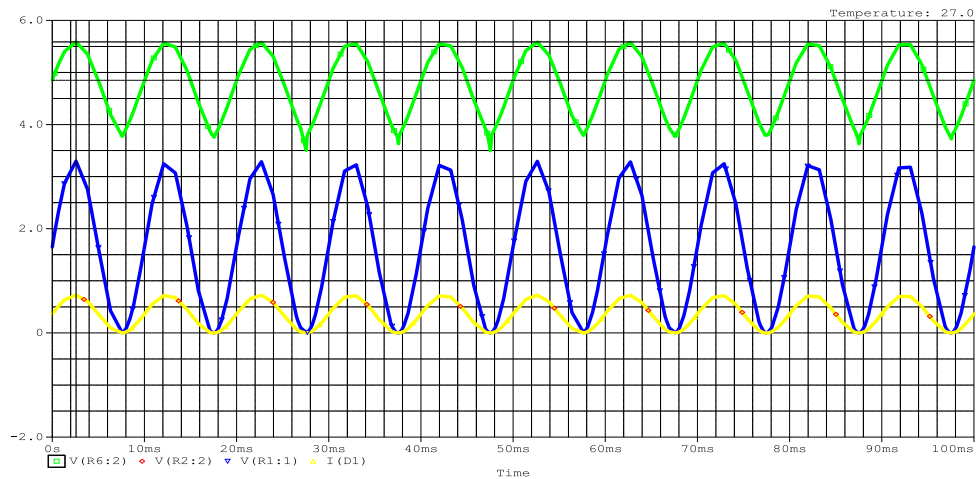


Figure B.2: 3W LED driver simulation. The yellow wave is the current flowing through the LED [A], the red line is the input voltage signal after the voltage divider [V]. The blue wave is the input signal from the signal generator (sinusoidal signal with 100 Hz frequency, 1.65 V amplitude and 1.65 V DC offset) [V] and the green wave is the output signal of the op-amp [V].

Lastly, Figure B.3 shows the first working prototype of the driver. The circuit is identical to the schematic shown in B.1. Unfortunately, no pictures of the measurements were taken.

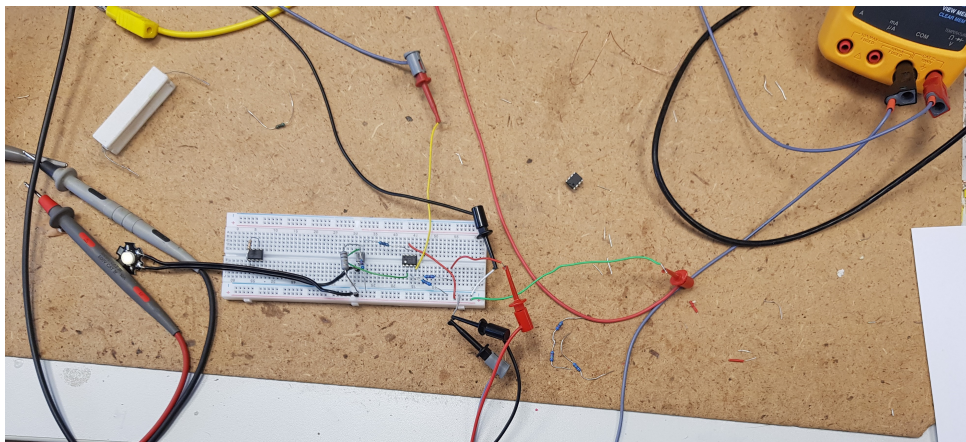


Figure B.3: 3W LED prototype.

Appendix C

LoRaWAN ABP communication

```
1  /*
2  LoRaABP.ino
3
4  Establish a connection on a LoRaWAN network in ABP mode.
5  Exchange data to/from the network.
6
7  Extract of the LoRaWAN standard:
8
9  Activation by personalization directly ties an end-device
10 to a specific network by-passing the join request
11 - join accept procedure.
12
13 Activating an end-device by personalization means that the
14 DevAddr and the two session
15 keys NwkSKey and AppSKey are directly stored into the end-
16 device instead of the DevEUI,
17 AppEUI and the AppKey. The end-device is equipped with the
18 required information for
19 participating in a specific LoRa network when started.
20
21 */
22 #include "src/LoRaWANNode.h"
23 #include "keys.h"
24
25 // #define FRAME_DELAY 300000 // in ms. Every 5 minutes by
26 // default.
27 #define FRAME_DELAY 20000 // 20s
28
29 // Serial port use to communicate with the USI shield.
30 // By default, use D0 (Rx) and D1(Tx).
31 // For Nucleo64, see "Known limitations" chapter in the README
32 // .md
33 HardwareSerial SerialLora(PC11, PC10);
34
35 // Device address, network & application keys
36 const char devAddr[] = DEV_ADDR;
37 const char nwkSKey[] = NWK_S_KEY;
38 const char appSKey[] = APP_S_KEY;
```

```

37 char frameTx[] = "UpAck!";
38
39 void setup()
40 {
41   Serial.begin(9600);
42   Serial.println("-- LoRaWAN ABP sketch --");
43   Serial.println(SerialLora);
44   // Enable the USI module and set the radio band.
45   while(!loraNode.begin(&SerialLora, LORA_BAND_EU_868)) {
46     Serial.println("Lora module not ready");
47     delay(1000);
48   }
49
50   // Set the network keys of the module
51   while(!loraNode.joinABP(devAddr, nwksKey, appSKey)) {
52     Serial.println("joinABP failed!!");
53     delay(1000);
54   }
55
56   Serial.println("Lora module ready\n");
57
58   String str = "Device address: ";
59   loraNode.getDevAddr(&str);
60   Serial.println(str);
61   str = "NwksKey: ";
62   loraNode.getNwksKey(&str);
63   Serial.println(str);
64   str = "AppSKey: ";
65   loraNode.getAppSKey(&str);
66   Serial.println(str);
67 }
68
69 void loop()
70 {
71
72   transmit();
73   receive();
74   delay(FRAME_DELAY);
75 }
76
77 void receive(void) {
78   uint8_t frameRx[256];
79   uint8_t len;
80   uint8_t port;
81
82   // Check if data received from a gateway
83   if(loraNode.receiveFrame(frameRx, &len, &port)) {
84     uint8_t n = 0;
85     //Serial.print("frame received: 0x");
86     while(len > 0) {
87       Serial.print(frameRx[n], HEX);
88       //Serial.print(frameRx[n]);
89       Serial.print(' ');
90       len--;
91       n++;
92     }
93     Serial.print(" on port "); Serial.println(port);

```

```
94     } else {
95         //Serial.println("No data received");
96     }
97 }
98
99 void transmit(void) {
100     // Send unconfirmed data to a gateway (port 1 by default)
101     int status = loraNode.sendFrame(frameTx, sizeof(frameTx),
102                                     UNCONFIRMED);
103     if(status == LORA_SEND_ERROR) {
104         Serial.println("Send online ack failed!!!");
105     } else if(status == LORA_SEND_DELAYED) {
106         Serial.println("Module busy or duty cycle");
107     } else {
108         Serial.println("Online ack sent");
109     }
110 }
```